DIPLOMARBEIT

Coupling of terahertz quantum cascade laser disks and ridges

durchgeführt von

Martin Janits

0127149

Malfattigasse 45/2/26

A-1120 Wien

am

Institut für Photonik

der Technischen Universtität Wien

unter der Leitung von

Univ.Prof. Mag.rer.nat. Dr.rer.nat. Karl Unterrainer

und

Dipl.-Ing. Christoph Deutsch

Wien, Juni 2011

Kurzfassung

Das Ziel der vorliegenden Arbeit ist die Untersuchung von Kopplungseffekten bei Terahertz Quantenkaskadenlasern (THz QCLs) mit unterschiedlichen Resonatorbauformen. Dieser wenig benutzte Frequenzbereich befindet sich zwischen Mikrowellen und dem mittleren Infrarotbereich. Halbleiterlaser sind die einzigen kompakten und kohärenten Strahlungsquellen in diesem spektralen Bereich und daher interessant für verschiedenste Anwendungen, wie zum Beispiel das Erkennen von Tumoren in der Medizintechnik oder bei Ganzkörperscannern in der Sicherheitstechnik. Die QCLs werden durch Heterostrukturen des GaAs/AlGaAs Materialsystems realisiert, das als aktives Verstärkermedium dient. Mittels Molekularstrahlepitaxie (MBE) wird diese aus 271 Kaskaden bestehende aktive Zone gewachsen. Die Laserniveaus entstehen durch quantenmechanisch gebundene Zustände in dieser gewachsenen Nanostruktur, welche es ermöglichen, optische Übergänge zu definieren. Zwischen diesen eng benachbarten Energie - Subbändern ist es schwierig, eine Besetzungsinversion herzustellen, die für die optischen Übergänge erforderlich ist. Dies wird durch ein resonantes Phononen Design erreicht, wobei das untere Laserniveau durch longitudinale optische (LO) Phononen sehr rasch entleert wird. Als Wellenleiter dienen zwei Metallschichten (DM) oberhalb und unterhalb des aktiven Materials. Für die QCLs werden Fabry - Pérot- und Disk - Resonatoren verwendet.

Zuerst wurden einzelne QCL Disk - Resonatoren mit unterschiedlichen Radien hinsichtlich ihrer Kennlinien charakterisiert und die aufgezeichneten Spektren mit den Simulationsergebnissen verglichen. Die Messungen zeigten, dass die Disk - Resonatoren hauptsächlich im Einzelmodenbetrieb THz - Strahlung emittieren und die spektralen Messergebnisse gut zu den simulierten Eigenfrequenzen passten. Anschließend wurden gekoppelte Disks mit unterschiedlichen Radien und Abständen zwischen den Resonatoren untersucht. Es zeigte sich, dass die optimale Zusammenstellung der Resonatorgrößen die Kopplung sehr stark beeinflusst und dadurch die Möglichkeit besteht, die Emission des Kopplungspartners zu steuern.

Gekoppelte QCL Fabry - Pérot Resonatoren wurden ebenfalls hinsichtlich ihrer Kopplung bei unterschiedlichen Längen und Abständen untersucht.

Abstract

The objective of the presented thesis is to study coupling effects of terahertz quantum cascade lasers (THz QCLs) with different resonators. This underused frequency region is situated between the microwaves and the mid - infrared region of the electromagnetic spectrum. Semiconductor lasers are the only compact and coherent radiation sources in this spectral region and therefore interesting for many applications, such as indication of tumors in the medicine technology of body scanners in the field of security technology. The QCLs are realized through a heterostructure of the GaAs/AlGaAs material system, which acts as active material. The active region, consisting of 271 cascades, is grown by molecular beam epitaxy (MBE). Laser levels in a QCL are formed by quantum mechanically bound states in the grown nanostructure, which allows us to define optical transitions. Population inversion is very difficult to establish between these closely adjacent energy subbands, which is necessary for optical transitions. The resonant phonon design is used for the QCLs, where the lower laser level is depopulated very quickly by longitudinal optical (LO) phonons. A double - metal (DM) waveguide, where the active medium is arranged in between two metal layers, is used. Fabry - Pérot (ridge) and disk shape resonators are used for the QCLs.

Single QCL disk resonators with different radii were characterized and the recorded spectra of the devices were compared with the simulation results. The measurements showed that single disk resonators emitting THz radiation mainly in single mode operation and the recorded spectra fitted very well to the simulations of the Eigenfrequencies. Coupled disks with different dimensions and gaps between the two disk resonators were investigated afterwards. The results showed, that the right combination of resonator sizes had a strong influence of the coupling between the two disks. Due to the coupling effect, it was possible to control the emission of one disk with the other one. The coupling effects of coupled QCL ridge resonators with different length and gap sizes were also analyzed.

Contents

1. Introduction

Terahertz (THz) radiation is an electromagnetic radiation with a frequency between the microwave and the infrared region of the electromagnetic spectrum. The THz band does not have a standard definition until now, but commonly used definitions are included in the spectral region between 100 GHz (0.1 THz) and 10 THz. It correlates to wavelengths from 3mm to 30 μm. This part remains the least explored region of the electromagnetic spectrum due to technical difficulties involved in building efficient, powerful and compact sources and detectors. The lack of suitable technologies established the phrase "THz gap" for this part of the spectrum.

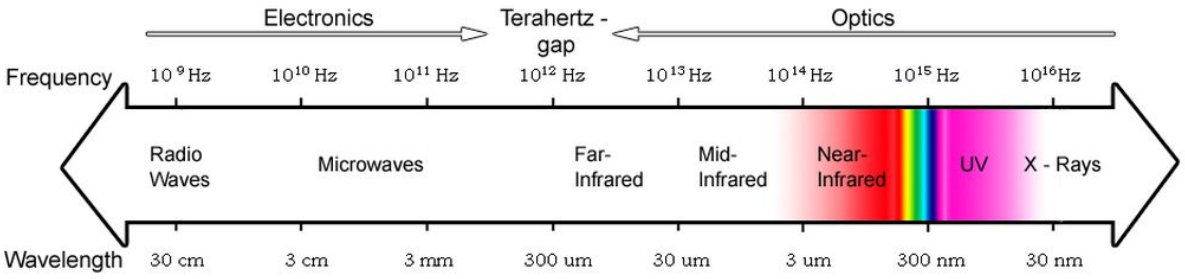

Figure 1.1.: The location of the THz region in the electromagnetic spectrum.

This THz gap is surrounded from two fundamentally different technologies. Reducing the size of electronic components leads to higher operation frequencies and approaches the gap from the electronics side. The other possibility to close the gap from the high frequency side is leading photonic devices to lower frequencies. Therefore a huge effort over the last two decades was necessary to expand the operation frequencies of electronic and photonic devices.

1.1. Applications

The THz spectral region has a lot of spectral features associated with fundamental physical processes. This can be rotational transitions of molecules, large-amplitude vibrational motions of organic compounds, lattice vibrations in solids and intraband transitions in semiconductors. THz applications use these unique characteristics of different material responses to THz radiation.

Material Type	Optical Property
liquid water	high absorption ($\alpha \approx 250cm^{-1}$ at 1 THz)
metal	high reflectivity (>99.9% at 1 THz)
plastic	low absorption ($\alpha < 0.5cm^{-1}$ at 1 THz) low refractive index (n≈ 1.5)
semiconductor	low absorption ($\alpha < 1cm^{-1}$ at 1 THz) high refractive index (n≈ 3.4)

Table 1.1.: Optical properties of different materials in the THz band (taken from [1])

Condensed matter is grouped into the three types water, metal and dielectric, based on the optical properties in the THz regime (see Table 1.1). These contrasts of THz properties are useful for many imaging applications. Water is highly absorptive in the THz region and this sensitivity is useful for medical applications, because in a biological system small changes in water content could indicate crucial defects, such as basal cell carcinoma (a common form of skin cancer) and other diseases [2] (Fig. 1.2).

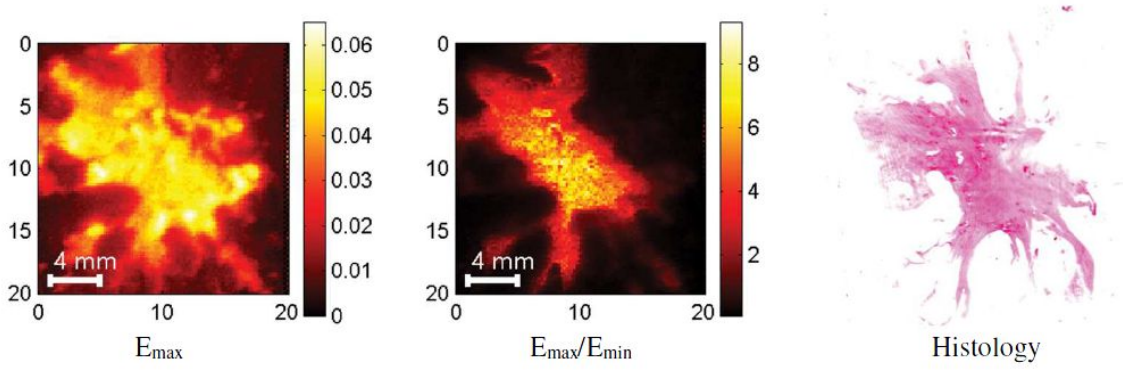

Figure 1.2.: Terahertz image of a freshly excised breast tissue. This figure shows two terahertz images generated using the maximum of the reflected pulse E_{max} (left) and the ratio between maximum and minimum of the reflected pulse E_{max}/E_{min} (middle). In the E_{max} image the tumor with surrounding adipose tissue is shown. In E_{max}/E_{min} only the tumor is visible and correlates well with the tumor shown in the histology image (right) (taken from [2]).

An advantage of these THz rays is that THz photons only carry small energies (in the order of meV) and are non-ionizing. Therefore these T-Rays (sometimes abbreviated analogous to X-Rays) are not harmful to DNA compared to X-Rays and are suitable for medical applications. Metals are highly reflective at THz frequencies, because of the high conductivity of the material, and can be easily identified by their complete opacity with THz imaging. Also spectral signatures of organic and biological molecules in the THz region are associated with intermolecular interactions and vibrational motions and these molecular dynamics are capable to analyze with THz spectroscopy[1].

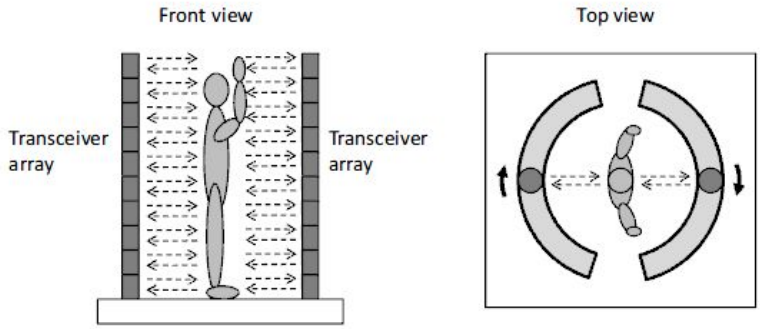

Figure 1.3.: Schematic diagram of a passenger imaging system (taken from [1]).

These concepts are applied to security applications to identify weapons, explosives and illegal drugs hidden behind typical wrapping and packaging materials (see Fig. 1.3 and Fig. 1.4). Nonpolar and nonmetallic materials, for example dielectrics such as paper, plastic, clothes, wood and ceramics, are transparent or low absorptive to THz radiation compared to optical wavelengths.

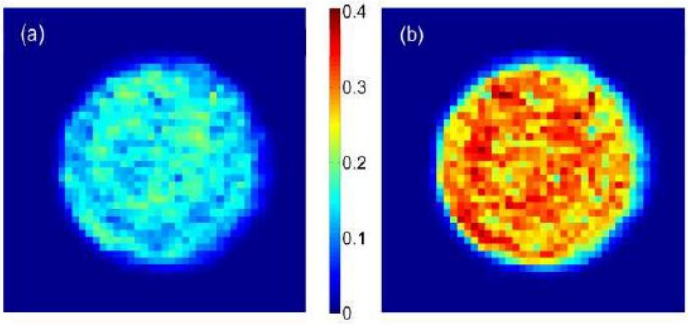

Figure 1.4.: Transmission images of a pellet containing 26-vol % of the high explosive pentaerythritol tetranitrate (PETN) taken at (a) 3.05 THz and (b) 3.24 THz (taken from [3]).

1.2. THz Generation and Detection

Technological advances in electronics and optics result in different types of THz sources and detectors.

Terahertz Sources:

One way of generating THz radiation is to take advantage of a nonlinear medium in which incident electromagnetic waves undergo a nonlinear frequency conversion.

Optical rectification is a second order nonlinear optical process. A THz photon at a specific frequency ω is created by interaction of two optical photons at frequencies $\omega 1$ and $\omega 2$ with a nonlinear crystal that $\omega = \omega 1$ - $\omega 2$. For an incoming femtosecond laser pulse with a broad spectrum a broadband THz pulse is generated through this process in the nonlinear crystal, whose shape is similar to the optical pulse envelope of the incoming femtosecond pulse.

Another method to produce THz radiation is difference frequency generation (DFG), which is also a second order nonlinear optical process. Two slightly detuned lasers are mixed in a nonlinear crystal where the difference frequency is in the THz range [4]. The significant difference to optical rectification is that DFG produces continuous wave (CW) THz radiation.

THz generation is also possible based on microwave technology. Incoming microwaves are converted into their harmonic waves making use of diodes with a strongly nonlinear I-V characteristic and generates CW THz radiation by frequency multiplication [1].

Accelerating charges and time-varying currents are also possible to radiate electromagnetic waves. THz radiation can be generated with a biased photoconductive (PC) antenna, which consists of two metal electrodes on a semiconductor substrate, excited by laser beams. The principle of this generation technique is that an optical beam, illuminating the gap between the electrodes of the PC antenna, generates photocarriers. A static bias field on the electrodes accelerates the free carriers and this photocurrent varies in time to the corresponding incident laser beam intensity. With this technique it is possible to generate broadband THz pulses from femtosecond laser pulses or mixing two laser beams with different frequencies forming an optical beat generating CW THz radiation at the beat frequency [1].

Far-IR gas lasers, typically pumped by a CO2 laser, utilize molecular rotation energy levels whose transition frequencies fall into the THz region [5]. The achievable output power with this gas lasers is in the order of hundreds of milliwatts at room temperature, but the whole system

is very huge and emitted only on a small number of discrete frequencies.

A quantum cascade laser (QCL) is a semiconductor heterostructure laser which generates CW THz radiation (described in Chapter 2.2). It is one of the best sources in the THz spectral region in terms of output power, linewidth and the possibility for integration due to the fact that it is a semiconductor source.

Terahertz Sensors:

THz detection schemes are classified as either coherent or incoherent detection techniques. The difference between this two methods is that coherent detection measures the amplitude and phase of the field, whereas incoherent detection only the intensity.

Coherent detection techniques are closely associated with the generation techniques. They share underlying mechanisms and key components, for example optical techniques as described above use the same light source for generation and detection.

Free space electro-optic (EO) sampling measures the actual electric field in the time domain of broadband THz pulses to make use of the Pockels effect. An incoming THz radiation induces birefringence, which is proportional to the incoming field, in a nonlinear optical crystal. A weak optical probe pulse measuring the field induced birefringence as a function of the relative time delay between the THz and the probe pulse.

With a PC antenna it is also possible to measure broadband THz pulses in the time domain. Photocarriers injected from an optical probe pulse induces a current in the photoconductive gap of the antenna dependent on the THz field amplitude. It is possible to reconstruct the pulseshape in the time domain of the incoming THz pulse by measuring the photocurrent while varying the time delay between the THz pulse and the optical probe pulse.

Incoherent detectors are thermal sensors such as bolometers, Golay cells and pyroelectric devices. The common feature of all these thermal detectors is a radiation absorber attached to a heatsink which measures the temperature increase. The advantage of these sensors is the broad measurement range of incoming radiation, but the detection response is relatively slow compared with typical light sensors because the radiation absorber must reach thermal equilibrium for temperature measurement [1].

1.3. Laser fundamentals

A laser (light amplification by stimulated emission of radiation) is a device that generates or amplifies coherent radiation. They come in a great variety of forms using different laser materials, atomic systems for the active medium and different kind of pumping or excitation techniques. With the possibilities of variation, lasers can amplify radiation at wavelengths ranging from the far infrared region up through the visible region of the electromagnetic spectrum and extended to the ultraviolet and even X-ray region [6].

The essential elements of every laser device are:

- a laser medium consisting of an appropriate collection of atoms, molecules, ions or a semiconductor crystal
- a pumping process to excite these atoms or molecules in the laser medium into a higher quantum mechanical energy level and create population inversion
- suitable optical feedback elements that allow a beam of radiation to either pass once through the medium or bounce back and forth repeatedly through the laser medium

The possible interaction of light with matter is described with a simple two level model. Figure 1.5 shows the distinction of three different cases for this interaction.

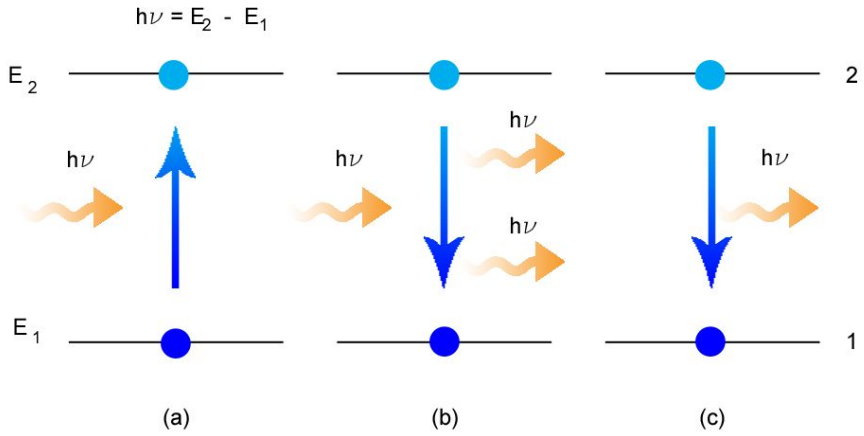

Figure 1.5.: Schematic illustration of the three light matter interactions in the active medium: (a) absorption, (b) stimulated emission, (c) spontaneous emission

An incoming photon with the energy $h\nu = E_2 - E_1$ is absorbed and elevates an electron to the

higher energy state E_2 (Fig. 1.5(a)). Another possibility is the spontaneous transition from an excited electron in the upper energy state E_2 to the lower state E_1 emitting a photon with the energy $h\nu$ (Fig. 1.5(c)). This process is called spontaneous emission of a photon, which propagation direction and phase is purely random.
An incoming photon can also trigger the electron transition from E_2 to E_1. The excited electron in the upper state is stimulated by an incident photon to relax to the lower state and emits another photon, which yields to a stimulated emission of a photon with $h\nu$ (Fig. 1.5(b)). This newly created photon has the same propagation direction, polarization, phase and spectral characteristics of the incoming photon. Stimulated emission is the fundamental process for amplification of light in a laser [6].

The probabilities for absorption and stimulated emission are equal. Population inversion is necessary to achieve light amplification by stimulated emission in the active laser medium. In this condition the upper laser level E_2 must be higher populated compared to the lower level E_1. The population inversion can be obtained by pumping the active medium with light (optically pumping) or electrically like in semiconductor heterostructure lasers or QCLs.
Due to the same probabilities for absorption and stimulated emission, population inversion in a two level system is impossible and only equal occupation states of the levels can be achieved by strong pumping. For that reason the active medium of a laser consists of a material system with at least three discrete energy states. A detailed description of the active medium in a THz QCL is given in Chapter 2.2.3.

2. Theoretical background

2.1. Semiconductor heterostructures

A semiconductor heterostructure consists of at least two dissimilar semiconductor materials. For the realization of such semiconductor heterostructures, abrupt material changes on the atomic scale are necessary. An atomically sharp interface results in a discontinuity in the energy bands of the two involved materials, which is required to engineer quantized transitions within the valence or the conduction band. Epitaxial crystal growth techniques, molecular beam epitaxy (MBE) (described in Chapter 4.1) for example, provide this atomic layer thicknesses control of the layer. The underlying physics of semiconductor heterostructures is matching of the lattice constant of the appropriate materials. Huge lattice mismatch causes dislocations and stress at the interface and results in electrical defects. The lattice constants and energy gaps E_g of commonly used semiconductors are shown in Figure 2.1.

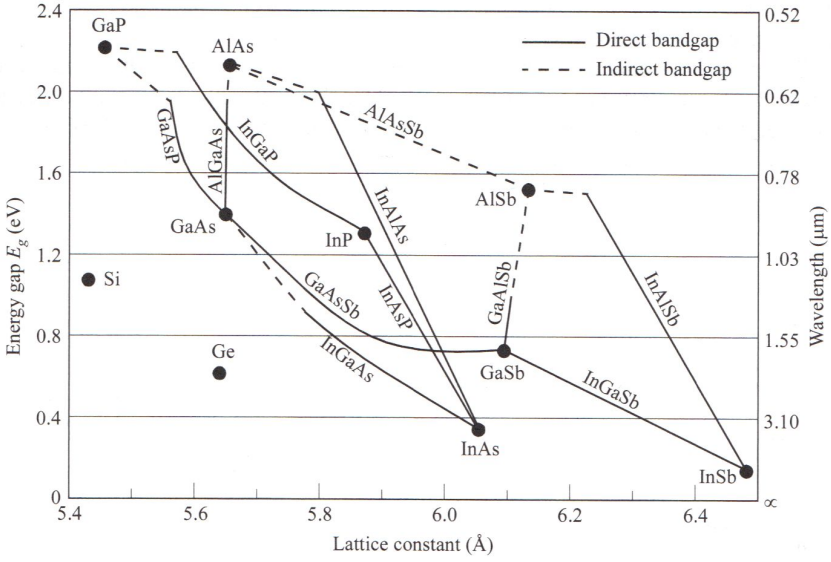

Figure 2.1.: Lattice constants and energy gap E_g for common semiconductors (taken from [7]).

A good combination for heterostructures are two materials of similar lattice constants and different energy gaps such as $GaAs/AlGaAs$. An advantage is also the availability of $GaAs$

substrates with high quality.

In addition to the different energy gaps of the materials, also the electron affinities of the semiconductors differs, which leads to different combinations of the valence and conduction band alignment at the interfaces. Due to their band alignment, heterostructures can be classified into three groups (Fig. 2.2).

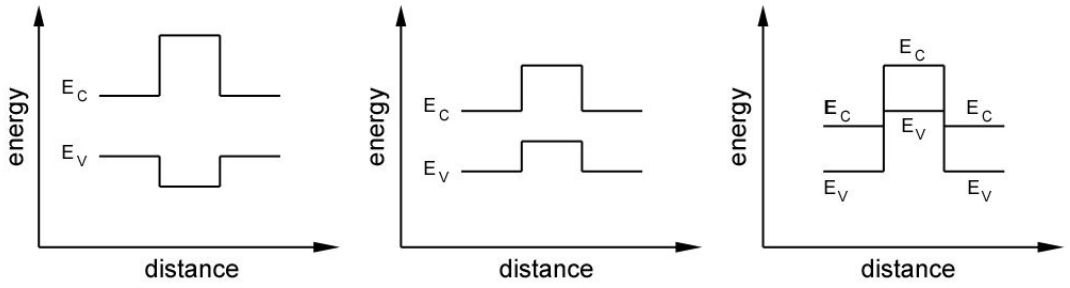

Figure 2.2.: Energy band diagram of a Type-I (left), Type-II (middle) and Type-III (right) heterostructure.

In a Type-I or straddling heterostructure one material has a lower conduction band energy E_C and a higher valence band energy E_V compared to the other junction material. Therefore, it must have a smaller energy gap E_g and the electrons and holes are confined in the same layer. In a Type-II or staggered heterostructure, the location of lower E_C and higher E_V are displaced. Electrons collected at lower E_C and holes collected at higher E_V are confined in different layers. Type-III or broken gap heterostructure is a special case of Type-II, where E_C of one material of the junction is lower than E_V of the other junction material [7].

2.1.1. Material system GaAs/AlGaAs

Optoelectronic devices often use semiconductor compounds from elements of the third group (In, Ga, Al) and the fifth group (As, Sb, P) of the periodic table with direct bandgaps. As we have seen in Figure 2.1, the $GaAs/AlAs$ system exhibits a really unique situation. The lattice constants of these two materials have almost identical values and differ only by 0.14%, independent of the aluminum content, which makes the system inherently lattice-matched. For $Al_xGa_{1-x}As$ $(0 \leq x \leq 1)$ layers grown on $GaAs$ the dielectric function and the optical gaps depend on the composition of aluminum content parameter x [8].

$Al_xGa_{1-x}As$ allows us to engineer the bandgap E_g of the bandstructure with the aluminum content x. Together with the lattice-matched $GaAs$ it is possible to create semiconductor

heterostructures of Type-I (see Fig. 2.2). Only for concentrations below approximately 45% (x=0.45), $Al_xGa_{1-x}As$ remains as a direct semiconductor like $GaAs$, otherwise it becomes indirect like $AlAs$. The basic parameters of both materials are shown in Table 2.1.

	$GaAs$	$AlAs$	$Al_xGa_{1-x}As$
crystal structure	zinc blende	zinc blende	zinc blende
a [Å]	5.6533	5.6611	5.6533 + 0.0078x)
E_g [eV] at 300K, $x \leq 0.45$	1.424	2.17	1.424 + 1.247x
E_g [eV] at 300K, $0.45 < x \leq 1$	1.424	2.17	$1.9 + 0.125x + 0.134x^2$
m_e^*/m_0	0.063	0.19	0.063 + 0.083x
m_{hh}^*/m_0	0.51	0.76	0.51 + 0.25x
m_{lh}^*/m_0	0.082	0.15	0.082 + 0.068x

Table 2.1.: Properties of $GaAs$, $AlAs$ and $Al_xGa_{1-x}As$ (taken from [9])

$GaAs$ and $Al_xGa_{1-x}As$ crystallizes in a zinc blende structure, where the two types of atoms form two interpenetrating face-centered cubic lattices. In Figure 2.3 the zinc blende structure and the band diagram of $GaAs$ is illustrated.

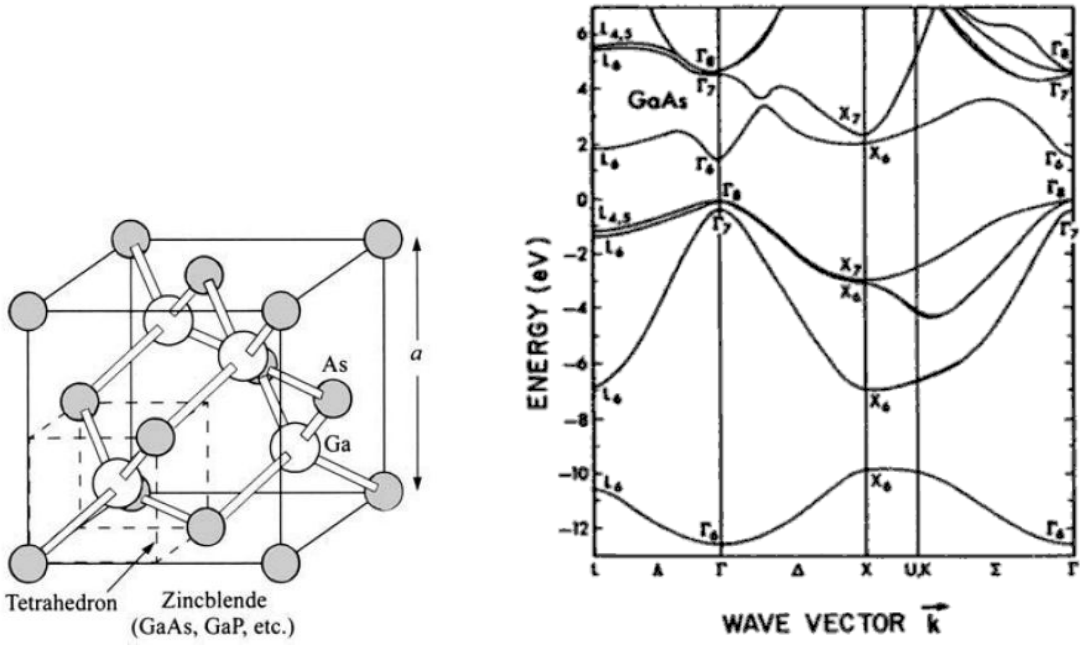

Figure 2.3.: Crystallographic structure of $GaAs$ (taken from [7]) and band structure of $GaAs$ (taken from [10]).

2.1.2. Electronic states

The electronic wave functions of a superlattice can be calculated over the envelope-function approach in the effective mass approximation [11]. The total wave function $\psi_i(r)$ is the product of the lattice-periodic Bloch function $u_\nu(r)$ of band ν and an envelope function $f_i(r)$, which is slowly varying over one lattice period.

$$\psi_i(r) = f_i(r)u_\nu(r) \tag{2.1}$$

In this equation, i is the quantum number of the particular state. The envelope function $f_i(r)$ depends on the shape of the superlattice structure potential and other external potentials such as electric and magnetic fields. A Schrödinger equation for the envelope function $f_i(r)$ can be derived with the assumption, that the lattice-periodic function is the same for all constituent materials.

$$-\frac{\hbar^2}{2m^*}\nabla^2 f_i(r) + V(r)f_i(r) = E_i f_i(r) \tag{2.2}$$

$V(r)$ is the potential, E_i the energy and m^* the effective mass of electrons. With z denoted as the growth direction,

$$f_{nk_\perp}(r) = \frac{1}{\sqrt{A}}e^{jk_\perp \cdot r}\varphi_n(z) \tag{2.3}$$

separates the motion of electrons perpendicular to z. A is the sample area and $k_\perp$ denotes the two dimensional vector (k_x, k_y). This separation reduces to a one-dimensional Schrödinger equation

$$-\frac{\hbar^2}{2m^*}\frac{d^2\varphi_n(z)}{dz^2} + V(z)\varphi_n(z) = E_n\varphi_n(z)\ , \tag{2.4}$$

which must be solved in each layer (A, B, ...) of the heterostructure. The solutions have to be connected with the matching conditions at each interface z_0:

$$\varphi^A(z_0) = \varphi^B(z_0) \tag{2.5}$$

$$\frac{1}{m^{*A}}\frac{d\varphi^A}{dz}(z_0) = \frac{1}{m^{*B}}\frac{d\varphi^B}{dz}(z_0) \tag{2.6}$$

The second condition ensures conservation of the probability current. Due to this, the envelope

function has a kink at each interface when the effective mass is discontinuous. The Schrödinger equation then reads

$$-\frac{\hbar^2}{2}\frac{d}{dz}\left[\frac{1}{m^*(z)}\frac{d}{dz}\varphi_n(z)\right] + V(z)\varphi_n(z) = E_n\varphi_n(z) \ . \tag{2.7}$$

The solution leads to energy Eigenvalues of the form

$$E_n(k_\perp) = E_n + \frac{\hbar^2 k_\perp^2}{2m^*} \ , \tag{2.8}$$

where the subband energies E_n are the quantized energy states in z-direction depend on the shape of $V(z)$. Electrons carrying an electric charge and therefore influence the shape of the conduction band. To consider this effect in the calculation, the poison equation has to be self consistently solved with the Schrödinger equation.

$$\frac{d}{dz}\left[\varepsilon(z)\frac{d}{dz}\phi(z)\right] = -\rho(z) \ , \tag{2.9}$$

where $\varepsilon(z)$ is the permitivity, $\phi(z)$ the electrostatic potential and $\rho(z)$ the space charge. The conduction band profile $E_c(z)$ is then calculated as

$$E_c(z) = E_{c0}(z) - e\Phi(z) \ , \tag{2.10}$$

where $E_{c0}(z)$ is the calculated conduction band without the influence of electric charges.

2.2. Quantum Cascade Laser

A quantum cascade laser (QCL) is a semiconductor heterostructure laser where periodically alternating layers of dissimilar semiconductor materials are forming a superlattice. The first working QCL was demonstrated in 1994 by Faist et al. [12], emitting in the mid infrared at a wavelength of 4 μm or 75 THz, respectively. The big advantage of the quantum cascade lasers is the ability of designing the properties of the laser. The active region parameters, e.g. the transition energies or the matrix elements, can be designed by bandstructure engineering. These properties are adjusted by varying the individual barriers and wells in the active region. The advantage in "designing" the laser was only possible by solving the problems on growing of the active region. It is necessary to control the thickness of the individual barrier and wells on a monolayer scale and establish comparable growth quality of layer thickness and interface between layers during the entire process. The design of a THz QCLs will be described in Chapter

4.2.

The basic operation of a QCL relies on the two essential processes intersubband transitions and cascading. In contrast to conventional diode semiconductor lasers, where the recombination of electron and hole pairs is radiative, an intersubband transition involves only one type of carriers within the conduction or the valence band. Therefore the intersubband process is called a unipolar process [1].

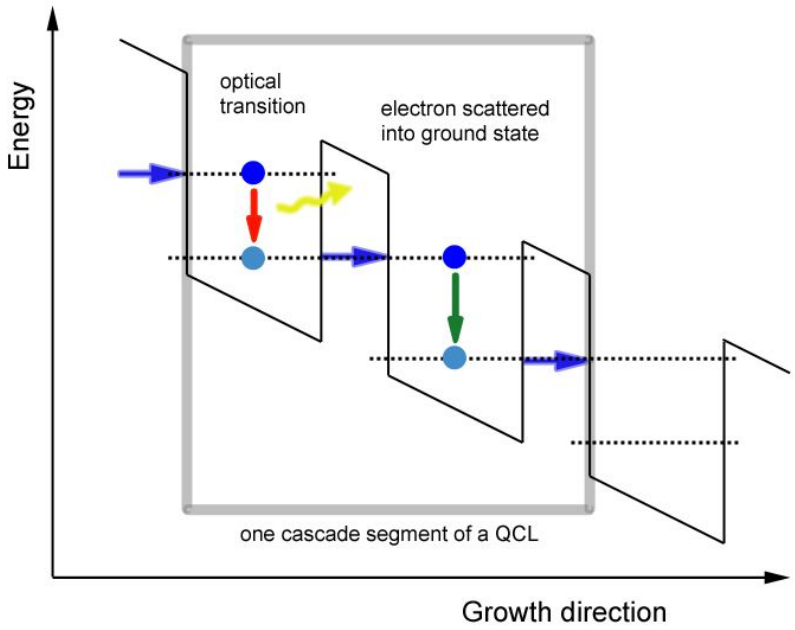

Figure 2.4.: Schematic of one cascade in a QCL.

In the superlattice structure an electron undergoes an intersubband transition in one period and the same electron is injected into the next period and subject to another intersubband transition, a schematic is shown in Figure 2.4. The term "cascading" reflects the repetitive nature of the multiple intersubband transitions until the electron reaches the end of the superlattice. The advantage of the cascading process is that multiple photons can be generated by a single electron [1].

Quantum cascade lasers have become an important source of coherent radiation in the mid infrared spectral region. They are able to operate in continuous wave (cw) mode with output powers up to several watts even at room temperature and above [13] [14].

For development of THz QCL are two difficulties to overcome. The first problem is that the energy of a 1 THz photon (4.1 meV) is so low that thermal excitations can disturb very easily the electron configuration, e.g. the population inversion which is necessary for lasing in a

QCL. The output power of the QCL falls of quickly as the temperature increases because the upper state lifetime is drastically reduced. Second, it is difficult to confine laser modes with the long wavelength of THz radiation in a small volume. Stimulated emission efficiency is proportional to the light intensity in the gain medium and therefore mode confinement is important [1].

The first THz QCL, emitting at 4.4 THz, was demonstrated by Köhler et al. [15] in 2002. As described above temperature performance is still an issue, THz QCL working up to 186 K in pulsed mode [16] and 225 K with an assisted magnetic field [17] was reported.

2.2.1. Radiative transitions

The optical gain in QCLs is provided by stimulated emission of photons from electron transitions between subbands in the heterostructure. In this section, the main steps for the derivation of stimulated and spontaneous emission rates are described [18]. The transition between two conduction subbands occurs at a probability rate, given by Fermi's golden rule:

$$W_{i\to f} = \frac{2\pi}{\hbar} \langle f, n_{q,\sigma}| H' |i, m_{q,\sigma}\rangle^2 \, \delta(E_f - E_i \pm \hbar\omega_q) \ , \tag{2.11}$$

where

$$H' = -\frac{e}{m^*} A \cdot p \tag{2.12}$$

is the interaction Hamiltonian. The initial $|f, n_{q,\sigma}\rangle$ and final states $|i, m_{q,\sigma}\rangle$ are product states of the conduction band envelope function eigenstates i and f and the photon eigenstates with n and m photons in each mode. The photon wavevector q at a frequency ω_q and the polarization state σ describes the photon eigenstates. m^* is the effective mass and A the Lorentz-gauge vector potential for a harmonic interaction in the equation for the Hamiltonian. Vector A can be written in term of the raising and lowering operators $a^\dagger_{q,\sigma}$ and $a_{q,\sigma}$:

$$A = \sqrt{\frac{\hbar}{2\varepsilon\omega_q V}} \hat{e}_{q,\sigma} (a_{q,\sigma} e^{jq\cdot r} + a^\dagger_{q,\sigma} e^{-jq\cdot r}), \tag{2.13}$$

where ε is the permittivity, V the cavity volume and $\hat{e}_{q,\sigma}$ is the polarization vector. We can adopt the electric dipole convention $e^{jq\cdot r} \approx 1$ for THz radiation ($\lambda > 10$ μm) and r in the order of the quantum well. The envelope wave functions vary spatially only in the growth z-direction. The scalar product of the momentum operator p in equation (2.12) can be reduced to

$$\hat{e}_{q,\sigma} \cdot p = (\hat{e}_{q,\sigma} \cdot e_z)\, p_z \ . \tag{2.14}$$

This product is only different from zero, if the polarization vector $\hat{e}_{q,\sigma}$ has a component in z-direction. It implies, that intersubband transitions are only allowed along the z-direction (TM polarized). Using the commutation relation for the unperturbed Hamiltonian H_0

$$\frac{j}{\hbar}\left[H_0, z\right] = \frac{p_z}{m^*} \ , \tag{2.15}$$

the matrix element follows as

$$|\left\langle f\right| p_z \left|i\right\rangle|^2 = \left(m^* \frac{E_f - E_i}{\hbar}\right)^2 |\left\langle f\right| z \left|i\right\rangle|^2 = \left(m^* \omega_q\right)^2 |z_{if}|^2 \ . \tag{2.16}$$

Inserting the matrix element into (2.11) give the following spontaneous and stimulated transition rates:

$$\begin{aligned} W_{if}^{spont} &= \frac{e^2 \pi \omega_q}{\varepsilon V} |\hat{e}_{q,\sigma} \cdot \hat{z}|^2 |z_{if}|^2 \delta\left(E_f - E_i + \hbar\omega_q\right) \ , \\ W_{if}^{stim} &= \frac{e^2 \pi \omega_q}{\varepsilon V} |\hat{e}_{q,\sigma} \cdot \hat{z}|^2 |z_{if}|^2 \delta\left(E_f - E_i + \hbar\omega_q\right) m_{q,\sigma} \ . \end{aligned} \tag{2.17}$$

Contrary to the spontaneous emission, the stimulated emission is dependent on the incident light field by the number of photons in mode $m_{q,\sigma}$.

2.2.2. Nonradiative scattering

The design of energy levels and wavefunctions allows scattering rates to be engineered to provide a population inversion. Therefore, understanding the scattering mechanism is essential for the design of a QCL. Longitudinal optical (LO) phonon scattering is the dominant mechanism for an electron in the upper subband to relax, if the subband spacing is larger than the LO-phonon energy E_{LO}. It can be used as a very efficient depopulation mechanism for the lower lasing level, if the spacing of the involved energy levels is designed accurately. If the energies of the lasing subbands are separated less than E_{LO}, other dominant scattering mechanisms contributes to the nonradiative relaxation. These are a combination of electron - electron (e-e) scattering, electron - impurity scattering and LO phonon scattering of the high energy tail of the subband electron distribution. Also other scattering processes exist, such as acoustic phonon scattering or interface roughness scattering, but they are often considered to be less important. In this section, a description of the LO phonon scattering mechanism is presented, because the H256 samples used for this thesis based on LO phonon depopulation for the lower lasing level.

Longitudinal optical (LO) phonon scattering

The formalism used below to describe the electron LO phonon scattering is taken from Smet [19]. If the energy difference between the subbands is larger than the LO phonon energy E_{LO} (36.25 meV for GaAs at the Γ-point), LO phonon scattering is the dominant intersubband scattering mechanism. The scattering rate for an electron initially in state $|i\rangle$ with the energy E_i to the final state $|f\rangle$ with E_f through an interaction potential H' is evaluated using Fermi's golden rule

$$W_{i\to f} = \frac{2\pi}{\hbar} \mid \langle f| H' |i\rangle \mid^2 \delta(E_f - E_i \pm \hbar\omega_{LO}) \ . \tag{2.18}$$

The electron-phonon interaction Hamiltonian has the form

$$H' = \sum_q \left[\alpha(q) \left(e^{jq\cdot r} b_q + e^{-jq\cdot r} b_q^\dagger\right)\right] \ , \tag{2.19}$$

where $\alpha(q)$ is the electron-phonon interaction and b_q and $b_q^\dagger$ are the creation and annihilation operators for a phonon in mode q. The Fröhlich interaction $\alpha(q)$ represents the strength of the scattering and is given by

$$\mid \alpha(q) \mid^2 = \frac{\hbar\omega_{LO}}{2} \frac{e^2}{q^2} \left(\frac{1}{\varepsilon_\infty} - \frac{1}{\varepsilon_{dc}}\right) \ , \tag{2.20}$$

with the high frequency permittivity ε_∞, the static permittivity ε_{dc} and the LO phonon energy $\hbar\omega_{LO}$. The factor $1/q^2$ suppresses scattering rates for large in-plane momentum differences. The highest scattering rate occurs, when the subbands are exactly separated by the LO phonon energy. Evaluation of the matrix element yields to a phonon emission rate of

$$\begin{aligned} W_{if} = {} & \frac{m_0^* e^2 \omega_{LO}}{8\pi\hbar^2} \left(\frac{1}{\varepsilon_\infty} - \frac{1}{\varepsilon_{dc}}\right) (n_{\omega_{LO}} + 1)) \\ & \times \int_0^{2\pi} d\vartheta \int dz \int dz' \phi_f(z)\phi_i(z)\phi_i(z')\phi_f(z') \frac{e^{-q|z-z'|}}{q^2} \ , \end{aligned} \tag{2.21}$$

where $n_{\omega_{LO}}$ represented the Bose-Einstein statistic. The integral represents the spatial dependence of the envelope function for the scattering process. If the subband energy difference is in the order of the LO phonon energy, calculations reveals scattering times in the sub-picoseconds range.

2.2.3. THz QCL active region designs

In THz QCLs the energy of the lasing transition is below the LO-phonon energy of the bulk material. The challenge is to obtain a population inversion between such closely spaced subbands by means of bandstructure engineering. Therefore other designs of the active region are necessary compared to mid-infrared QCLs.

Chirped superlattice design

The first published THz QCL by Köhler et al. [15] in 2002 was based on the chirped superlattice (CSL) design. The chirped superlattice active region is based on coupling of several quantum wells together to create minibands of states, when an appropriate electric field is applied (Fig. 2.5). Radiative transition takes place from the lowest state of the upper miniband '2' to the top state of the lower miniband '1'. A population inversion is established through the favored scattering of electrons between the tightly coupled states within the miniband. Therefore electrons tend to relax to the bottom of the minibands leaving the lower radiation states relatively empty. Due to the relatively small width of the minibands of about 15 - 20 meV, LO-phonons are not directly involved in the depopulation process, only thermally activated LO-phonon scattering is possible.

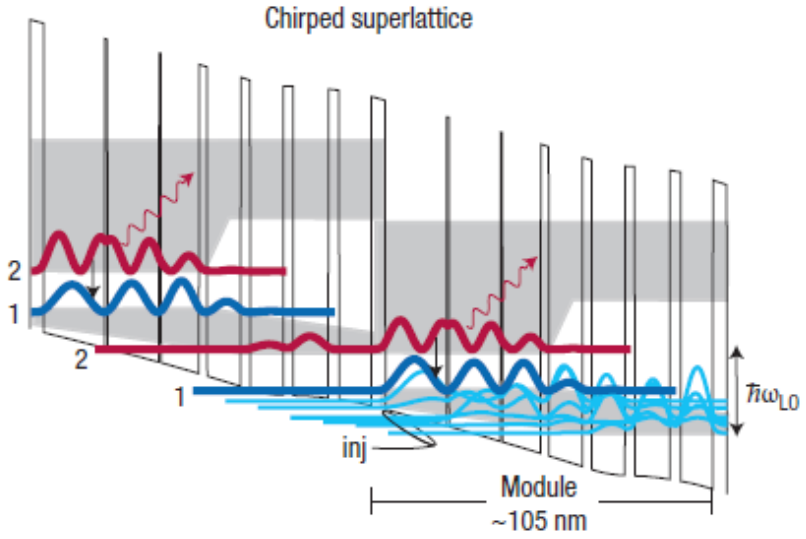

Figure 2.5.: Chirped superlattice design (taken from [20]).

Bound to continuum design

In the bound to continuum (BTC) design, the lower radiative state and the miniband based depopulation remains the same compared to the chirped superlattice design. An additional subband forming the upper laser state is introduced in the minigap. This upper state is essentially made to be a bound defect state in the minigap, with the effect, that the radiative transition is more diagonal in space (Fig. 2.6). The oscillator strength of the transition drops slightly compared to the CSL design, but the upper state lifetime increases as non-radiative scattering is reduced. The injector states couple more strongly with the upper state then with the lower miniband, resulting in a more selective injection process [20].

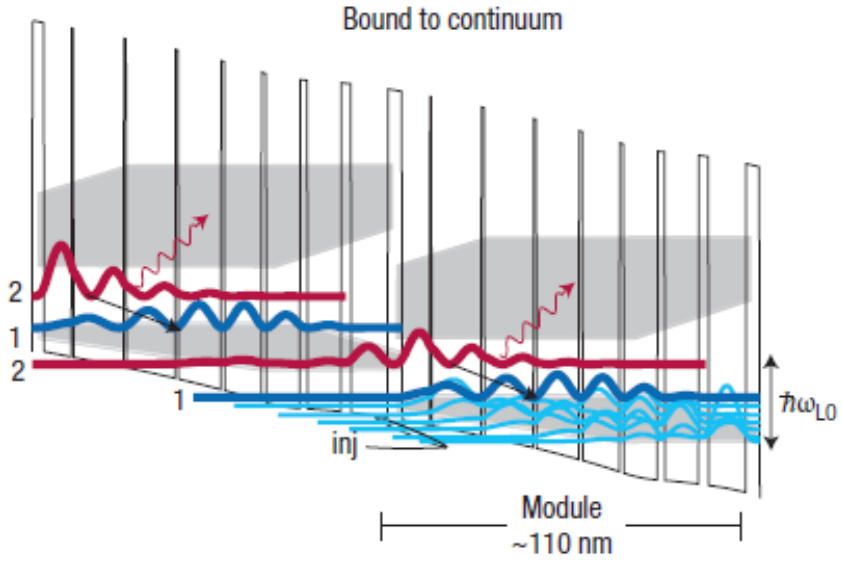

Figure 2.6.: Bound to continuum design (taken from [20]).

LO phonon design

Another major THz active region design is the resonant phonon (RP) scheme based on LO phonon depopulation for the lower laser state. It was first presented by Williams et al. [21] in 2003.

In the most common mid-infrared QCLs, collector and injector states are designed to be below the lower radiative state '1' by approximately $E_{LO} = 36$ meV. Due to this energy difference scatter the electrons in the lower laser state very quickly into the injector states by emitting an LO-phonon. Because of the close subband energy spacing in THz QCLs, it was difficult to

use LO-phonon scattering to depopulate the lower radiation state without also populating the upper state. The key development of the RP design was bringing the lower radiative state '1' into tunneling resonance with the excited state in the adjacent wells. Through this resonance the wavefunction is spread over several quantum wells, maintains a strong spatial overlap with the injector states and experiences subpicosecond LO-phonon scattering. The upper state '2' remains localized and has very little overlap with the injector states. This suppresses scattering and preserves lifetime in the upper state '2' of several picoseconds (Fig. 2.7) [20].

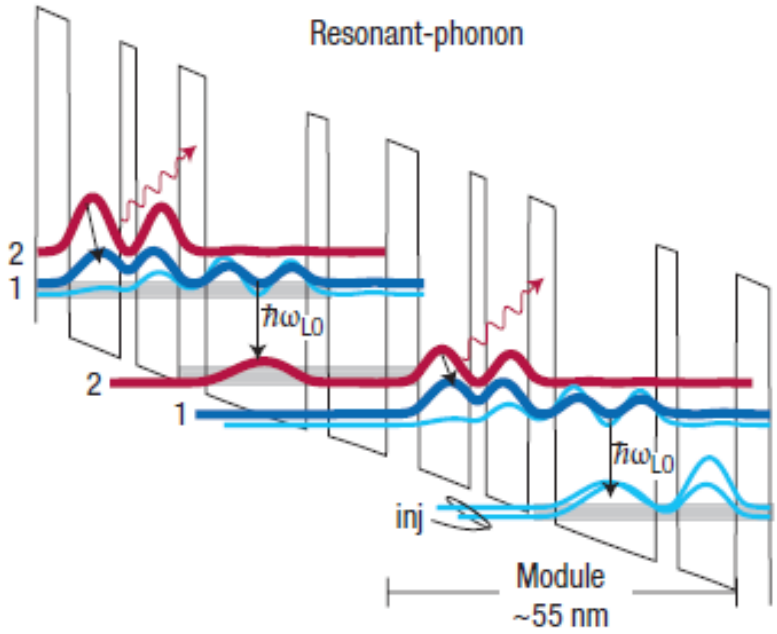

Figure 2.7.: LO phonon design (taken from [20]).

2.2.4. Sample H256

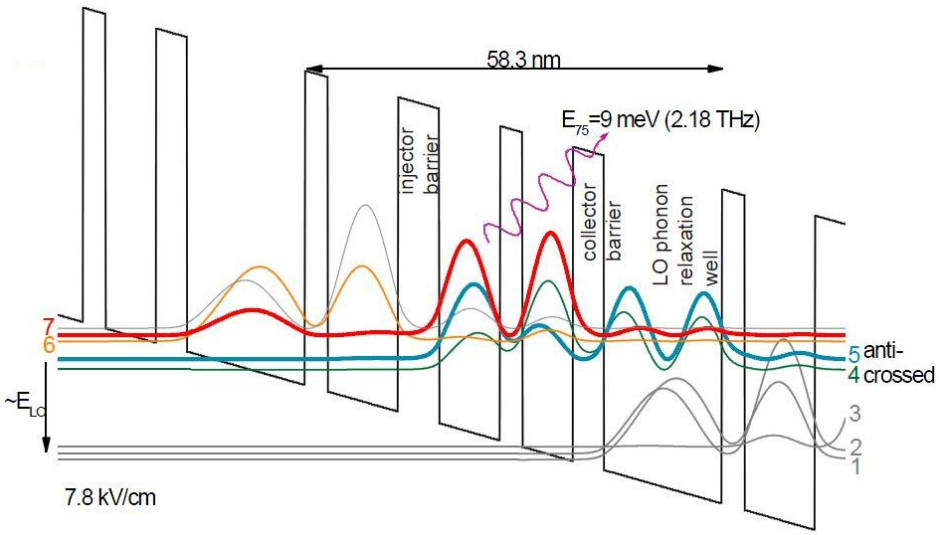

Figure 2.8.: Sample H256: Conduction band diagram of the layer sequence at an electric field of 7.8kV/cm with the moduli squared of the envelope function. The thickness of the barriers and wells are (starting at the injection barrier) **32**/97/**57**/84/**31**/70/**43**/163 (in $\AA$), barriers indicated in bold font. The calculations are performed with respect to the X-ray diffraction analysis, +1.0 % over-grown and an Al fraction of 15.6%. The 163 $\AA$ thick LO phonon relaxation well is doped with a concentration of $3.5 \cdot 10^{15}\ cm^{-3}$.

The active region of the H256 sample used in this diploma thesis is based on a LO phonon design. Figure 2.8 illustrates the one dimensional Schrödinger solver simulation results of the active medium for an electric field of 7.8 kV/cm. The simulated conduction band diagram shows the lower lasing states **4** and **5**, which are anti-crossed. This means, that the energy difference ΔE_{54} becomes a minimum and the matrix element a maximum at this bias field. The upper lasing states are **6** and **7**. The design enhances the lifetime of this upper laser levels by expanding the wavefunctions over several wells to bring the lower radiative state to tunneling resonance with the adjacent injector state. To ensure efficient depopulation of the lower laser states **4** and **5**, the energy difference between them and the upper laser states of the next cascade **1**, **2** and **3** must be in the order of the LO phonon energy. Strong spatial overlap of the lower lasing level with the next injector state provides a fast depopulation, while the upper level does not overlap and therefore has long lifetimes. Lasing transition occurs vertical within one well between the states **7** and **5**, because the matrix element Z_{75} is large at the designed field compared to the other matrix element Z_{65}. The subband **3** is expected to play a minor role for the transport since it is bypassed by the LO phonon scattering mechanism. The calculation yields to a radiative transition of 2.18 THz for this LO phonon design.

2.3. Terahertz waveguide concepts

Quantum cascade lasers were first realized only in the mid-infrared range based on dielectric waveguides [12]. Dielectric waveguides provide mode confinement and overlap with the active region using the refractive index difference between a high index layer sandwiched between lower index cladding layers. The propagation characteristics of such dielectric waveguides are only preserved, if the layer thicknesses scale linearly with the effective wavelength of the radiation in those media.
For longer radiation wavelength, two problems occur to maintain this resonator concept. Due to the small refractive index contrast, the cladding layers thicknesses has to be in the order of the wavelength which leads to long growth times by MBE. The second problem is the increase in loss due to the free carrier absorption. The QCLs are electrically pumped and require highly doped layers for electrical contact. This is important, because any leakage of the radiation field into these highly doped layers increases the waveguide loss. The free carrier absorption scales with λ^2, therefore the overlap with the highly doped contact layers has to be minimized.

To prevent these disadvantages, plasmon enhanced waveguides were developed for longer wavelength mid-infrared lasers [22][23]. By including a doped plasma layer, which plasma frequency approaches the laser frequency, the refractive index drops to due to anomalous dispersion. Through this doped layer between the top metal contact and the cladding layer, the required thickness of the cladding layer was reduced to realistic growth capabilities of the MBE process. A further development was the surface plasmon waveguide, which top metal contact is directly deposited on the active region. The advantage of this scheme was the drastically reduced layer thickness and the higher confinement factor. In the double-sided surface plasmon waveguide a heavily doped layer was included between the active region and the bottom substrate instead of the bottom cladding layer. This design of double - sided surface plasmon was taken one step further by making a double - metal waveguide for QCLs with higher wavelength [24].
In this work only double metal waveguides are used and therefore only this waveguide is described in Chapter 2.3.2.

2.3.1. Surface plasmons

Semi-insulating (SI) surface plasmon and the double-metal (DM) waveguide are the only commonly used waveguide concepts for THz QCLs. Both waveguides are based on surface plasmons. Surface plasmons are waves propagating along the surface of a conductor. Free electrons in the conductor interact with the light waves and confine the wave on the surface. The interaction consists of collectively oscillating of the free electrons in resonance with the light wave (Fig. 2.9(a)). These interdependency between the surface charge density and the electromagnetic field results in the momentum $\hbar k_{SP}$ of the surface plasmon mode greater than that of a free space photon of the same frequency $\hbar k_0$. Maxwell's equation solved with the appropriate boundary conditions leads to the frequency dependent surface plasmon wave-vector k_{SP}, which is also known as dispersion relation (Fig. 2.9(c)).

$$k_{SP} = k_0 \sqrt{\frac{\epsilon_d \epsilon_m}{\epsilon_d + \epsilon_m}} \tag{2.22}$$

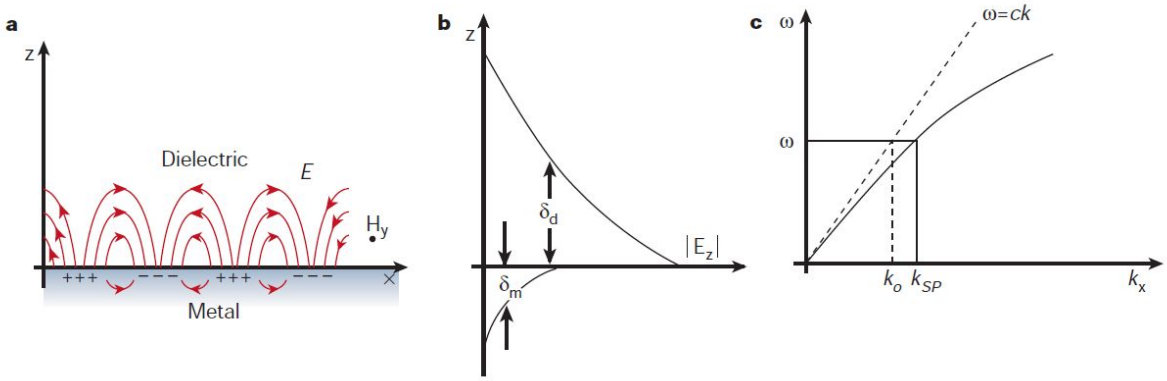

Figure 2.9.: Surface plasmon between a metal and a dielectric material.(a) Surface charge requires an electric field normal to the surface and a transverse magnetic (TM)field character. (b) Evanescent field in the perpendicular direction reflecting the bound, non-radiative nature of the surface plasmon and prevents power from propagating away from the surface. δ_d and δ_m are the decay lengths of the related materials. (c) Dispersion curve for a surface plasmon mode always lying beyond the light line and shows the momentum mismatch problem that must be overcome to couple light and surface plasmon modes (taken from [25]).

Surface plasmons are possible at a metal - dielectric interface, if the frequency dependent permittivity of the metal ϵ_m and the dielectric material ϵ_d have opposite signs. This condition is fulfilled for metals where ϵ_m is negative and complex. In contrast to the propagating nature of

surface plasmons along the surface the field perpendicular decays exponentially with distance from the surface. The perpendicular field is evanescent preventing power propagating away from the surface (Fig. 2.9(b)). A surface plasmon mode propagating on a metal surface will be attenuated due to losses from absorption in the metal. This depends on the dielectric function of the metal at the oscillation frequency of the surface plasmon.
Seeking the imaginary part k''_{SP} of the complex surface plasmon wavevector $k_{sp} = k'_{SP} + ik''_{SP}$ from the surface plasmon dispersion equation leads to the propagation length δ_{SP}

$$\delta_{SP} = \frac{1}{2k''_{SP}} = \frac{c}{\omega}\left(\frac{\epsilon'_m + \epsilon_d}{\epsilon'_m \epsilon_d}\right)^{\frac{3}{2}} \frac{(\epsilon'_m)^2}{\epsilon''_m}, \tag{2.23}$$

where ϵ'_m and ϵ''_m are the real and imaginary parts of the dielectric function $\epsilon_m = \epsilon'_m + i\epsilon''_m$ of the metal used for the surface plasmon propagation [25].

2.3.2. Double - metal waveguide

The two main building blocks of a laser are the active region and the optical cavity. Light is amplified in the active region by stimulated emission of intersubband transitions and the cavity has to confine the light. The optical cavity consists of the waveguide confining the light in the active medium and the positive feedback and outcoupling due to resonator. In this section the double - metal waveguide is described and resonator concepts are presented in the following chapters.
The first employment of a double - metal waveguide for QCLs was demonstrated in 2002 by Unterrainer et al. [26] operating in the mid-infrared range. This waveguide consists of the active medium sandwiched between two metal layers (Fig. 2.10(a)). These metal top and bottom layers act as waveguide and also as electrical contacts. At the interface between the metal and the semiconductor a surface plasmon can develop confining the mode between the metal layers (Fig. 2.10(b)).

This kind of waveguide provides a confinement factor Γ near unity, which is defined as

$$\Gamma = \frac{\int_{active} \Re(\vec{E} \times \vec{H}) \cdot \vec{e}_x dz}{\int_{resonator} \Re(\vec{E} \times \vec{H}) \cdot \vec{e}_x dz}\ , \tag{2.24}$$

where E is the electric- and H the magnetic field component of the light. The confinement factor Γ indicates the spatial overlap of the optical mode with the active medium in order to be

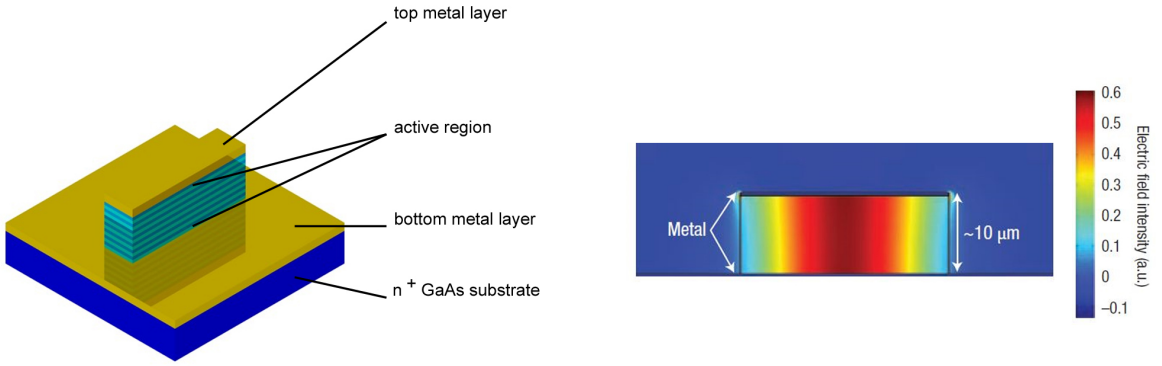

(a) (b)

Figure 2.10.: Double - metal waveguide (a) Schematic diagram (b) two-dimensional mode intensity patter (taken from [20])

amplified. If the wave reproduces itself after one round trip in the cavity, which means that the gain and the losses of the waveguide α_w and the mirror α_m are balanced, the threshold condition for lasing is satisfied [20].

$$\Gamma g_{th} = \alpha_m + \alpha_w \tag{2.25}$$

For double - metal waveguides, the mirror losses α_m are negligible for long resonators compared to the waveguide losses α_w. The waveguide loss coefficient α_w accounts for scattering and absorption inside the waveguide.

Double-metal waveguides tend to have better performances at higher temperatures, but lower output power and poor beam output patterns compared to semi-insulating surface plasmon waveguides. The reflectivity of the facet in double-metal waveguides is calculated by impedance mismatch of the subwavelength mode at the waveguide facet with free space propagation modes.

$$R = \left(\frac{Z_w - Z_a}{Z_w + Z_a} \right)^2 \tag{2.26}$$

Z_w and Z_a are the impedances of the waveguide and the free space ($Z_a = 377\Omega$). Depending on the waveguide dimensions relative to the wavelength, double-metal waveguides exhibit enhanced facet reflectivities up to $R = 0.9$. Due to these relatively small mirror losses smaller threshold current densities J_{th} and higher operating temperatures are reached. The strong mode confinement in double - metal waveguides enables vertical and lateral dimensions to be smaller than the wavelength. This reduces the total thermal dissipation and required cooling power for THz QCLs, which enables improved continuous wave (cw) operation [27][28].

For laser frequencies above 3 THz the choice of the waveguide depends on the intended use. At lower frequencies, the performance of SI surface plasmon waveguides breaks down dramatically and double-metal waveguides are the only realistic choice [29].

2.3.3. Ridge resonators

The simplest type of an optical resonator is a Fabry Pérot cavity (Fig. 2.11). It consists of two, plane parallel mirrors where at least one of the two has to be semi-transparent to couple the light out of the resonator. The reflectivity can be calculated over

$$R = \left(\frac{n_r - n_0}{n_r + n_0}\right), \tag{2.27}$$

where n_r is the refractive index of the semiconductor material and n_0 is the refractive index of the surrounding medium. The reflectivity originates from the difference of the refractive index of the semiconductor and air.
Standing waves forms inside the optical resonator, if they follow the condition

$$m = \frac{2L}{\lambda_{eff}}, \tag{2.28}$$

where λ_{eff} is the effective wavelength in the gain medium, L the resonator length and $m \in \mathbb{N}$. λ_{eff} can be calculated to

$$\lambda_{eff} = \frac{\lambda_0}{n_{eff}}, \tag{2.29}$$

with the vacuum wavelength λ_0 and the effective refractive index n_{eff}. Multiple wavelengths are possible to exist in the cavity with a frequency mode spacing of

$$\Delta f = \frac{c_0}{2n_{eff}L}. \tag{2.30}$$

The material constants for $GaAs$ and air achieve a reflectivity of about 30% at the facet. Together with the cavity length L the optical mirror loss can be shown to be

$$\alpha_m = \frac{1}{2L} ln(R_1 R_2). \tag{2.31}$$

Light is confined in the lateral direction by total internal reflection by removing all of the surrounding material.

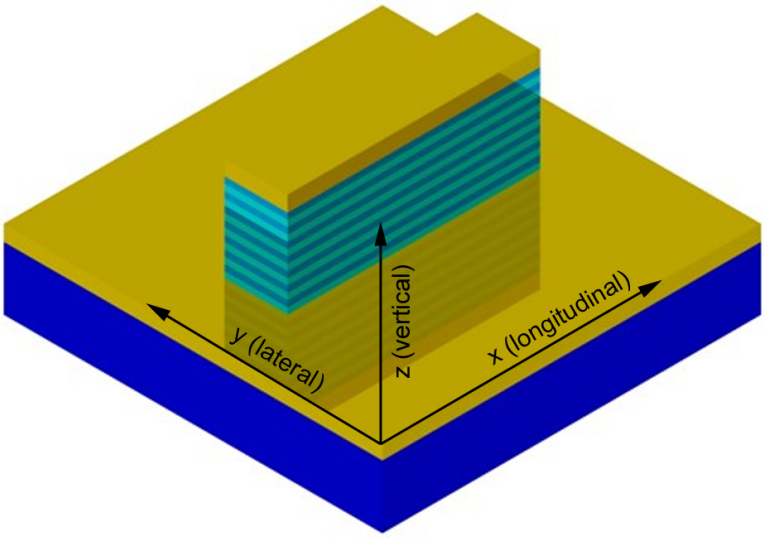

Figure 2.11.: Schematic diagram of a ridge resonator. The two parallel mirrors in the longitudinal direction form the Fabry Pérot resonator.

2.3.4. Disk resonators

Another attractive resonator type for QCLs operating in the THz frequency region is a cylindrical shaped resonator (Fig. 2.12). The first double-metal microdisk THz QCLs were demonstrated by Fasching et. al [30] in 2005, operating in the frequency region between 3.0 and 3.7 THz.

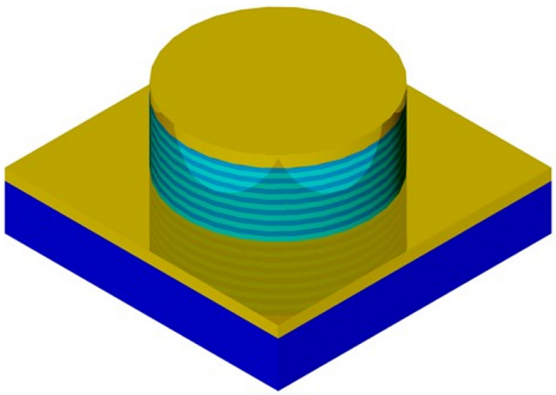

Figure 2.12.: Schematic diagram of a disk resonator.

In cylindrical shaped resonators two different mode types are supported to maintain optical

feedback for stimulated emission. The first mode type is called radial mode with the wave motion along the radial direction. Whispering-gallery modes (WGMs) are the second mode type where the light is confined by the total internal reflection at the outer perimeter of the gain medium due to the impedance mismatch between the waveguide and surrounding air.
The field distribution can be calculated by solving the Helmholtz equation

$$\left[\nabla^2 + n^2 k_0^2\right] \vec{E}(r,\omega) = 0 \ , \tag{2.32}$$

where n is the refractive index, $k_0 = \frac{\omega}{c_0}$ the wavevector in vacuum and $\vec{E}(r,\omega)$ the electric field vector as a function of the spatial coordinate r and the frequency ω. If we neglect the in-plane component of the TM polarized electric field, which means that the electric field vector is only considered in the growth direction, the equation can be simplified to

$$\left[\nabla^2 + n^2 k_0^2\right] \vec{E_z}(r,\omega) = 0 \ . \tag{2.33}$$

This equation transformed into cylindrical coordinates (r, φ, z) results in

$$\vec{E_z}(r,\varphi,z) = R(r)\Phi(\varphi)e^{-j\kappa z} \ , \tag{2.34}$$

where κ is the propagation constant in z-direction. Due to the double metal waveguide, where the active medium is between metallic contacts, ideal metallic boundary conditions are assumed. The compact design with a small height of the resonator compared to the wavelength taken into count, that only the lowest order mode in vertical direction is sustained. This simplification leads to the electric field component

$$E_z(r,\varphi) = A_m J_m(\frac{2\pi n_{eff} r}{\lambda_{n,m}})e^{jm\varphi} \ , \tag{2.35}$$

where A_m is a normalization constant, J_m are the Bessel functions of the first kind with $m \in \mathbb{Z}$ and $\lambda_{n,m}$ is the resonance wavelength.

$$\lambda_{n,m} = \frac{2\pi R n_{eff}}{x_{n,m}} \tag{2.36}$$

The resonance wavelength contains the disk radius R and $x_{n,m}$, which is the nth zero of the Bessel function J_m. The possible modes in such a disk resonator are characterized by the radial mode number n and the azimuthal mode number m. $m \gg n$ are ideal WGMs located close

to the outer rim of the gain medium and $n \gg m$ are ideal radial modes located close to the center of the gain medium. Each mode with (n, m) has $2m$ intensity maxima in azimuthal and n maxima in radial direction.

Disk resonators have smaller mirror losses than Fabry Pérot resonators and can be neglected compared to the double - metal waveguide losses. Due to the total internal reflection in disk resonators, the mode confinement is higher compared to Fabry Perot resonators. The radiation from a QCL disk can clearly be attributed to the more favorable whispering gallery modes [31].

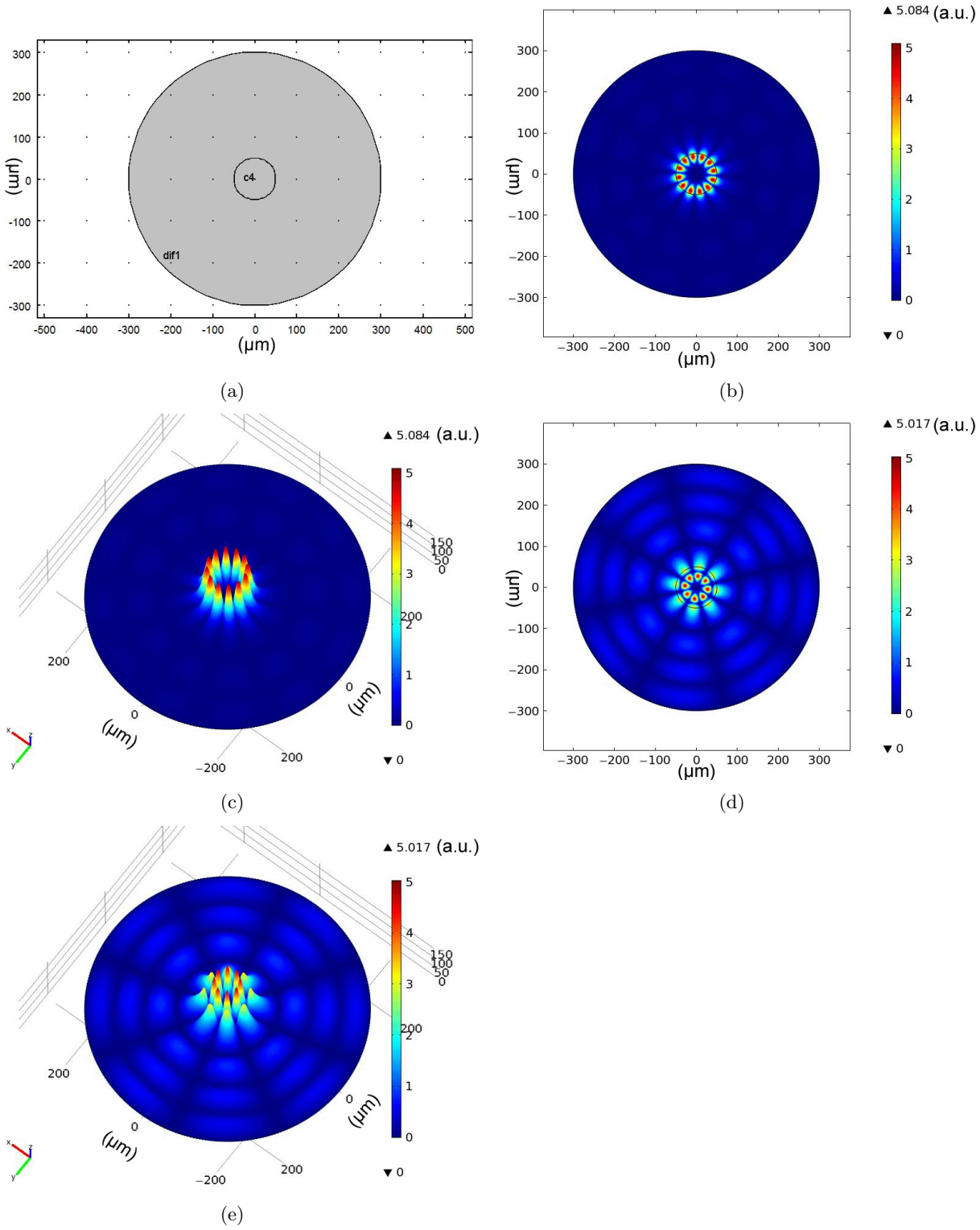

Figure 2.13.: 2D COMSOL Multiphysics simulations of whispering gallery modes of a disk resonator. (a) Radius of the disk $R = 50\mu m$ with effective refractive index $n_{eff} = 3.6$ surrounded with air ($n_{eff} = 1$). Whispering gallery modes with mode (n, m) are illustrated in: (6,1) in (b) and (c); (4,2) in (d) and (e).

3. Coupling of lasers

Coherent coupling between two QCL cavities is based on an enhancement of the optical output power under conservation of the inherent properties of a single QCL device. Due to the coupling, a gain in wavelength selectivity and mode stabilization is achievable. Applications like beam steering and far field shaping can also be realized by utilizing the effect of coupled QCL cavities. In principle are two different approaches possible of coupling between laser cavities. Evanescent field coupling describes the interaction of the cavities via a narrow coupling gap. Another possible method is direct coupling, where the devices touching each other and the modes are forced to couple. The present Chapter will give a discussion of evanescent field coupling which was realized in this thesis.

Evanescent field coupling

The formalism used below to describe the coupling coefficient of two semiconductor ridge lasers is taken from Agrawal [32]. Figure 3.1 shows two independently driven Fabry Pérot resonators, which are optically coupled through their mutual feedback. The static and dynamic characteristics of the coupled cavities are governed by a set of rate equations obtained after generalizing the correspondent single cavity equations.

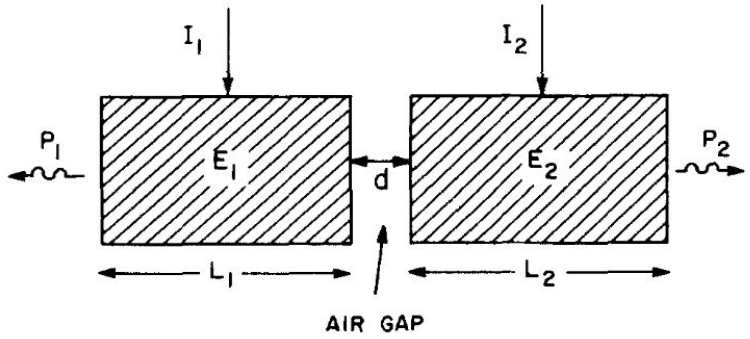

Figure 3.1.: Schematic illustration of coupled cavity semiconductor laser provided by an air gap of width d (taken from [32]).

Assuming single longitudinal mode operation and neglect spatial variations in the plane wave approximation, the optical field in each cavity is written as

$$\mathscr{C}_j(z,t) = \frac{1}{2}[E_j(t)e^{-i\omega t} + E_j^*(t)e^{i\omega t}]sin(k_j z), \tag{3.1}$$

where j equals 1 or 2 corresponding to the cavity, ω is the laser frequency, $k_j = \bar{\eta}_j\omega/c$, c is the vacuum velocity of light and $\bar{\eta}_j$ is the effective refractive index experienced by the laser mode. The (complex) field amplitude E_j and the carries density n_j in each cavity satisfy the rate equations

$$\frac{dE_j}{dt} = \frac{i\bar{\eta}_j}{\eta_{gj}}(\omega - \Omega_j)E_j + \frac{1}{2}(G_j - \gamma_j)(1 - iR)E_j + \gamma_j\kappa_j E_{3-j}, \tag{3.2}$$

$$\frac{dn_j}{dt} = \frac{I_j}{qV_j} - \left(\frac{n_j}{\tau_j} + \frac{G_j|E_j|^2}{\hbar\omega}\right). \tag{3.3}$$

In this equations, $\Omega_j = m_j\pi c(\bar{\eta}_j L_j)$ is the cavity resonance frequency with the integer m_j, $G_j = \Gamma_j\nu_{gj}g_j$ is the stimulated emission rate and $\gamma_j = \nu_{gj}\alpha_j$ is the photon decay rate. Further, $\nu_{gj} = c/\eta_{gj}$ is the group velocity calculated from the group index η_{gj}, g_j is the local gain and $\alpha_j = \alpha_j^m + \alpha_j^{int}$ includes the mirror loss α_j^m and the internal loss α_j^{int}. The antiguiding parameter R is defined as

$$R = \frac{\Delta\eta^{'}}{\Delta\eta^{''}}, \tag{3.4}$$

where $\Delta\eta = \Delta\eta^{'} + i\Delta\eta^{''}$ is the refractive index change due to injected carriers. In the carrier density equation 3.3 is I_j the device current, V_j the active volume, q the magnitude of the electronic charge and τ_j the total recombination time dependent of the carrier density. The dimensionless coupling coefficient κ_j can be calculated as

$$\kappa_j = \frac{1}{2\alpha_j L_j}\left(\frac{t_c}{r_c}\right), \tag{3.5}$$

where t_c and r_c are the complex transmission and reflection coefficients of the coupling element. The complex parameter $t_c/r_c = Te^{i\theta}$ shows that T and the phase θ vary significantly with the air gap width d. Therefore, the phase θ plays a major role in mode selection in a coupled cavity ridge laser.

Another possible configuration is based on evanescent field coupling between the high-Q whispering gallery modes of individual microdisk cavities [33]. Sufficiently large separation between the individual resonators is assumed that the resonators are weakly coupled. With the tight-binding approximation, the Eigenmode $E_K(r,t)$ of the coupled resonator optical waveguide (CROW) is a linear combination of the high-Q modes $E_\Omega(r)$ of the individual resonators along a straight line parallel to e_z (Fig. 3.2).

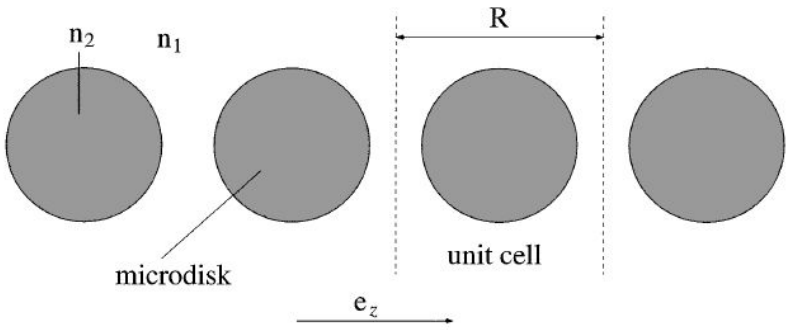

Figure 3.2.: Coupled resonator optical waveguide due to coupling between individual microdisks, with the size of a unit cell R and e_z as direction for periodicity (taken from [33]).

The Eigenmode for the center of the nth resonator $z = nR$ is written as

$$E_K(r,t) = E_0\, exp(i\omega_K t) \sum_n exp(-inKR) \times E_\Omega(r - nRe_z), \tag{3.6}$$

which satisfies the Bloch theorem and $E_\Omega(r)$ is assumed to be nondegenerated. Consequently the wave vector K is limited to the first Brillouin zone $-\pi/R \leq K \leq \pi/R$. $E_K(r,t)$ satisfies the Maxwell equations and leads to

$$\nabla \times (\nabla \times E_K) = \epsilon(r)\, \frac{\omega_K^2}{c^2}\, E_K, \tag{3.7}$$

where $\epsilon(r)$ is the dielectric constant of the coupled system and ω_K the Eigenfrequency of the waveguide mode. $E_\Omega(r)$ also satisfies Eq.(3.7) with the dielectric constant of a single resonator $\epsilon_0(r)$ and the single resonator mode frequency Ω instead of ω_K. After substituting the above equations, the dispersion relation for the waveguide $E_K(r,t)$ is

$$\omega_K^2 = \Omega^2\, \frac{1 + \sum\limits_{n\neq 0} exp(-inKR)\beta_n}{1 + \Delta\alpha + \sum\limits_{n\neq 0} exp(-inKR)\alpha_n}, \tag{3.8}$$

where α_n, β_n and $\Delta\alpha$ are defined as

$$\alpha_n = \int d^3r\epsilon(r)E_\Omega(r)\cdot E_\Omega(r-nRe_z), \qquad n\neq 0, \tag{3.9}$$

$$\beta_n = \int d^3r\epsilon_0(r-nRe_z)E_\Omega(r)\cdot E_\Omega(r-nRe_z), \qquad n\neq 0, \tag{3.10}$$

$$\Delta\alpha = \int d^3r[\epsilon(r)-\epsilon_0(r)]E_\Omega(r)\cdot E_\Omega(r). \tag{3.11}$$

For a sufficiently weak coupling between the resonators only the nearest neighbor coupling is considered, i.e. $\alpha_n = 0$ and $\beta_n = 0$ if $n \neq 1, -1$. Symmetry considerations requires that $\alpha_1 = \alpha_{-1}$ and $\beta_1 = \beta_{-1}$. Assuming that α_1, β_1 and $\Delta\alpha$ are small, Eq. (3.8) simplifies to

$$\omega_K = \Omega\left[1 - \frac{\Delta\alpha}{2} + \kappa_1\, cos(KR)\right], \tag{3.12}$$

where we define the coupling factor κ_1 as

$$\kappa_1 = \beta_1 - \alpha_1 = \int d^3r\left[\epsilon_0(r-Re_z) - \epsilon(r-Re_z)\right]\times E_\Omega(r)\cdot E_\Omega(r-Re_z). \tag{3.13}$$

This dispersion relation defines a photonic band by the coupling of the high-Q modes in the individual resonators.

4. Sample fabrication and measurement setup

4.1. Molecular beam epitaxy

Molecular beam epitaxy (MBE) is a technique to grow doped and undoped semiconductor materials and thin films down to monolayer size on a suitable substrate. Epitaxial techniques allow more flexibility in the growth and placement of semiconducting layers compared to other techniques such as bulk crystal growth, ion implantation and diffusion. The substrate acts as a template and has usually the same crystal structure and lattice constant between atoms, which are necessary for high quality crystalline grown layers. The quality of MBE grown epitaxial layers is much higher than that of the substrate. As a result crystal defects in the substrate can propagate into an epitaxial layer, therefore active layers of a device are grown after growth of a suitable thick "buffer" layer that filters out those defects [34].

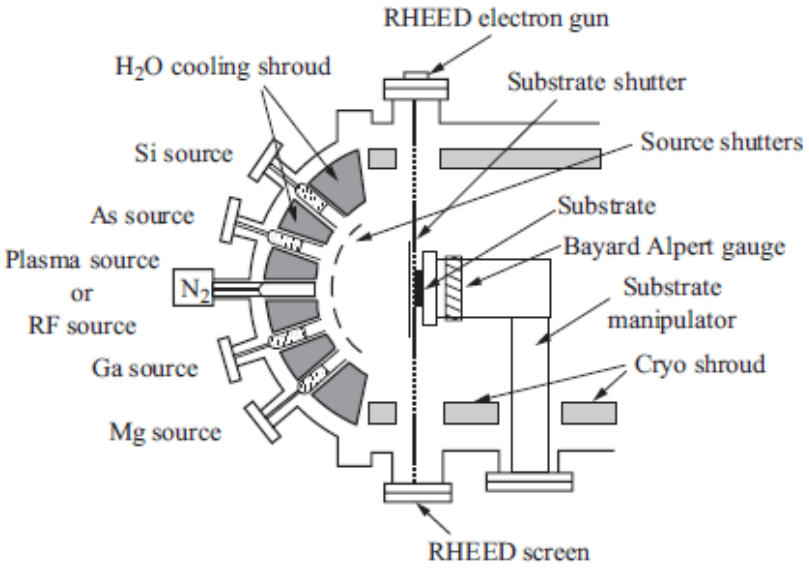

Figure 4.1.: Schematic illustration of the essential parts of a MBE growth system [35].

The essential elements of a molecular beam epitaxy system are illustrated in Figure 4.1. Each MBE arrangement may be splitted into three zones where different physical phenomena take place. In the first zone the molecular beams are generated under ultrahigh vacuum (UHV)

conditions. Next is the second zone where the beams from different material sources intersect each other. In this area the vaporized elements mix together creating a very special gas phase contacting the substrate. The third zone of the MBE physical system is that area where the crystallization processes on the substrate takes place.
The composition of the grown epilayer and its doping level depend on the relative arrival rates of the constituent material elements and dopants, which in turn is dependent on the evaporation rates of the different material sources. To start and stop the deposition and doping the beam fluxes are interrupted by simple mechanical shutters in front of the material beam sources. This mechanism allows abrupt changes in composition and doping on an atomic scale. A typically growth rate of 1 μm/h, which corresponds to 1 monolayer/s, is low enough for surface migration and leads to a very smooth surface of the growing film on the substrate.
The unique advantage of MBE, because it is realized in an ultrahigh vacuum environment, is the capability to monitor the growth process during operation with surface diagnostic methods in the chamber such as Reflection High-Energy Electron Diffraction (RHEED) or Auger Electron Spectroscopy (AES) [36].

A schematic picture of an active region grown with MBE is shown in Figure 4.2. The substrate of the sample is a semi insulating (SI) GaAs wafer with a thickness of approximately 650 μm. As described above to smoothen the surface and reduce crystal defects in the sample a 300 nm thick GaAs buffer layer is deposited followed by a 150 nm $Al_{0.55}Ga_{0.45}As$ etch stop layer, which is required for the double - metal processing of the waveguide (see Chapter 4.2). After a doped n^+ GaAs contact layer, 271 cascades of GaAs and $Al_{0.15}Ga_{0.85}As$ are grown and build the active region. The structure is finished on top again with a doped n^+ GaAs contact layer and an n^+ InGaAs layer with 50%In. This InGaAs layer allows higher doping than GaAs and acts as an ohmic contact.
X-ray diffraction is used to control the quality of the grown samples related to real thickness, uniformity of the cascades and aluminum content of layers. The growth sheet for the H256 material system, which was used for the coupled QCL samples, can be found in Appendix A.

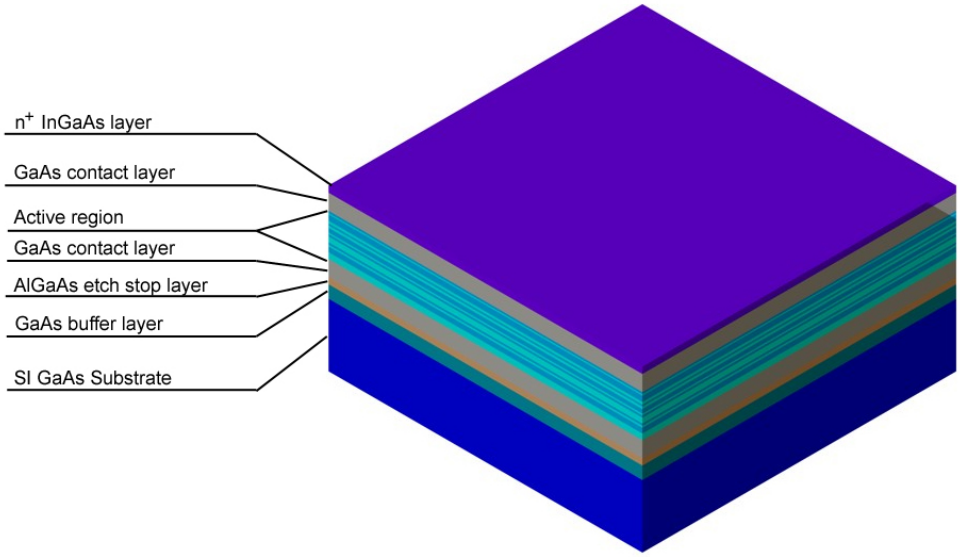

Figure 4.2.: Molecular beam epitaxy fabricated active zone of a QCL.

4.2. Double - metal processing

In this section the main double - metal processing steps realized in the cleanroom are listed. A more detailed description is given in the Appendix at the end of this diploma thesis (cleanroom recipe). In Figure 4.3, a schematic overview of these processing steps is shown. The process steps for disks and ridges are identically, only different masks for lithography are used.

The wafer grown with MBE is cleaved into approximately 1 cm^2 pieces and n^+ doped GaAs samples, which act as a receptor substrate, are cleaved slightly larger (Fig. 4.3(a)). Both samples are covered with a layer ($\approx 1\ \mu m$) of gold by a sputter process (Fig. 4.3(b)). Afterwards an Au-Au thermocompression bonding is performed in a commercial wafer bonder of type EVG 501. Therefore the MBE grown sample is flipped upside down onto the n^+ doped carrier sample and the stacked samples are bonded under heat and high pressure (Fig. 4.3(c)). In the next step the GaAs device substrate is lapped (mechanical polishing process) to a thickness of 50 μm. The remaining substrate is removed by a selective etching process with NH_4OH:H_20_2 stopping at the AlGaAs etch stop layer (Fig. 4.3(d)). The etch-stop layer is removed separately by 38% HF to expose the active region (Fig. 4.3(e)).

The structure of the Fabry-Pérot and disk resonators are defined by photolithography and a

following image reversal step (Fig. 4.3(f)). A gold layer is deposited on the top of the sample and after the lift-off process the top contact of the QCL structure remains (Fig. 4.3(g)). Finally, the resonators are formed by reactive ion etching (RIE), where the Au top contact acts as an etch mask. The RIE process removes the active material unless the bottom Au-layer is reached (Fig. 4.3(h)).

QCLs formed by a RIE process provide good results on steep sidewalls and surface roughnesses below 1 μm (Fig. 4.4). The processed samples are cleaved into appropriate pieces and soldered with indium on a piece of copper. This copper plate acts as a heatsink and as a carrier for the electrical connections. Therefore a contact pad is also glued onto this copper plate and connected via bonded gold wires to the QCL devices.

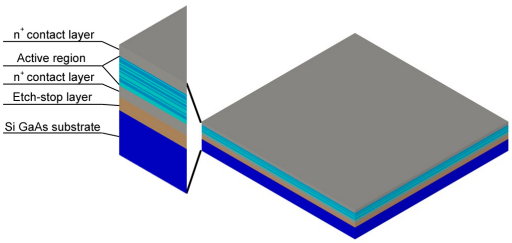

(a) SI substrate and grown MBE structure

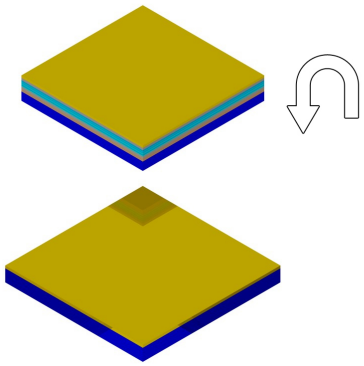

(b) Metallization for waferbonding process

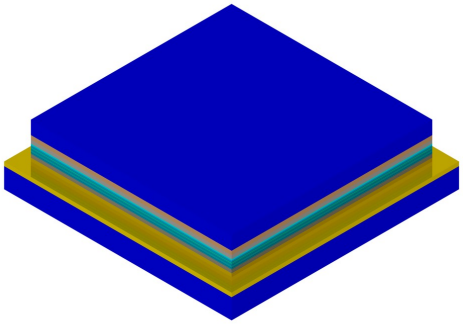

(c) Bonding process

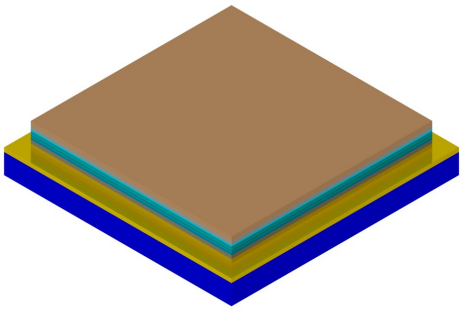

(d) Remove substrate

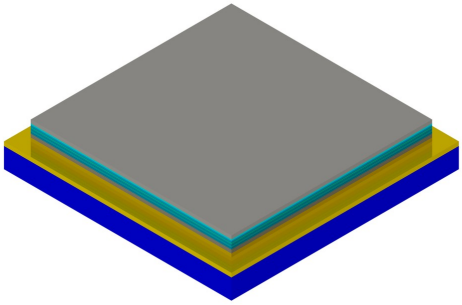

(e) Remove etch stop layer

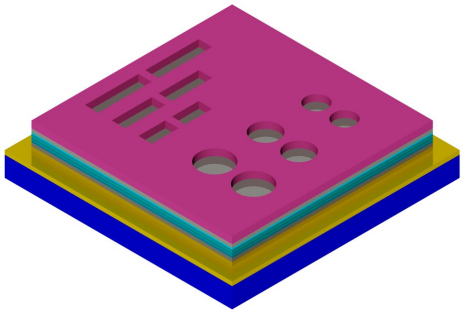

(f) Photoresist for lift- off process of top contacts

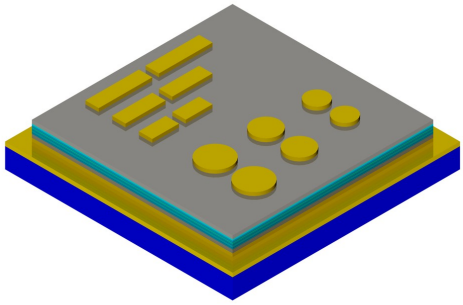

(g) Sputtering top contact / lift off process

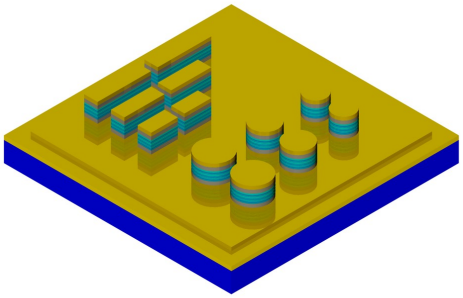

(h) Final double-metal structure after RIE etching

Figure 4.3.: Double - metal processing of laser ridges and disks.

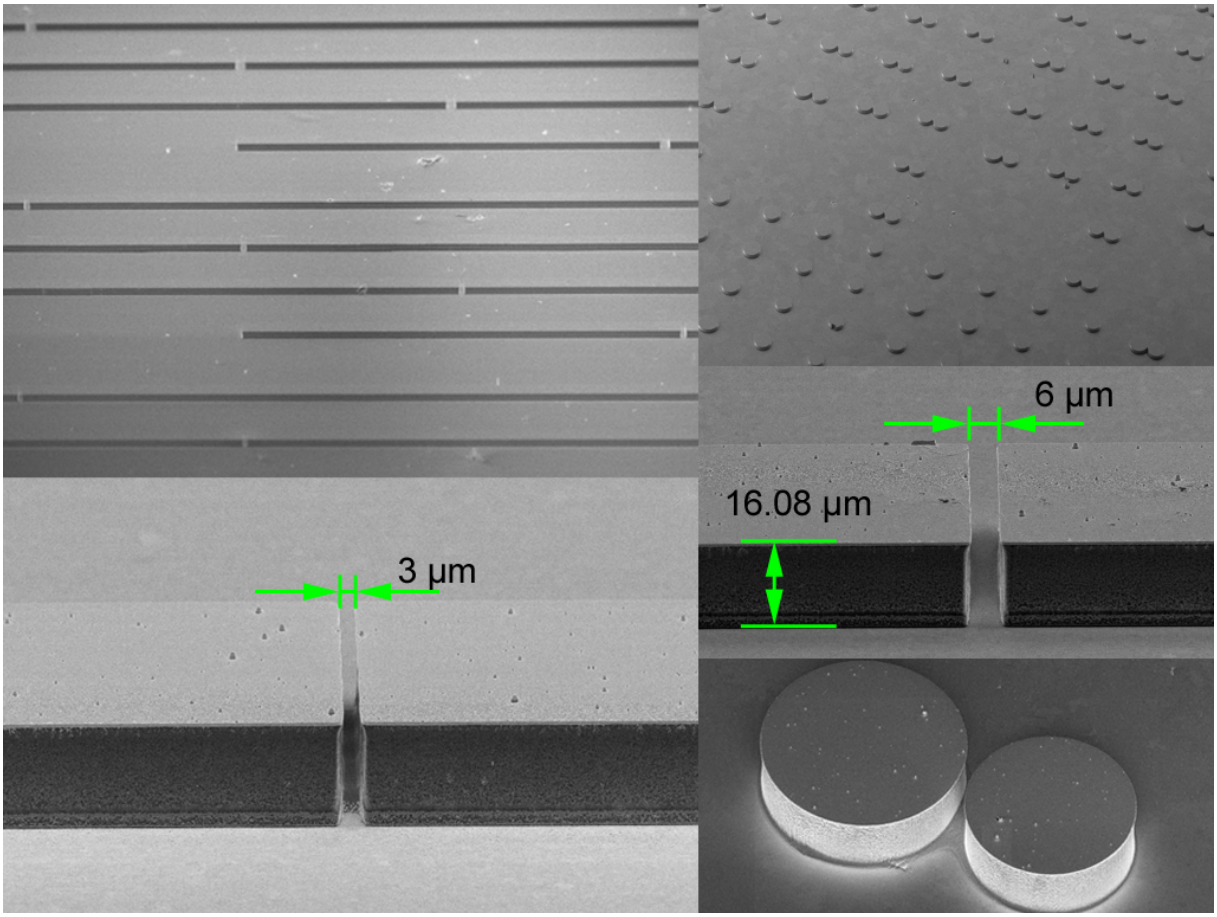

Figure 4.4.: SEM Pictures of processed double - metal ridges and disks.

4.3. Measurement setup

To perform the measurements two different setups have been used. One setup was used for the integral measurements at very low temperatures, which included current versus voltage (I-V) and current versus light (L-I) measurements for single (Chapter 4.3.3) and also coupled QCLs (2D-measurements) (Chapter 4.3.4). The second setup was used for spectral measurements for single and coupled QCLs (Chapter 4.3.5). In the following sections of this chapter these two setups and their major components are described.

4.3.1. Ge - Detector

To maximize the detectivity and quantum efficiency of extrinsic photoconductors, the doping level should be as high as possible, because the wavelength spectral cutoff is a function of the impurity doping density. The p-doped germanium detector (Ge - detector) is a photoconductive detector with a spectral range from approximately 1.8 THz to 9 THz. Photoconductive means the conductivity change caused by radiation exposure of the detector material. Ga doped ger-

manium - photoconductors are the best low background photon detectors for the wavelength range from 40 to 120 μm [37] with typical values of quantum efficiency from 10 to 20 %. The limit of useful doping which is possible in conventional extrinsic detectors is set by the onset of impurity banding. This occurs at sufficiently high doping levels and the wavefunctions of neighboring impurities overlap, their energy level is broadened to a band. The impurity banding effect limits the detector resistance and the photoconductive gain. To overcome these negative effects, blocked impurity band (BIB) devices were proposed [38].

BIB devices made from gallium doped germanium are sensitive to wavelength range located between 50 and 220 μm [39]. Figure 4.5 shows a BIB detector structure.

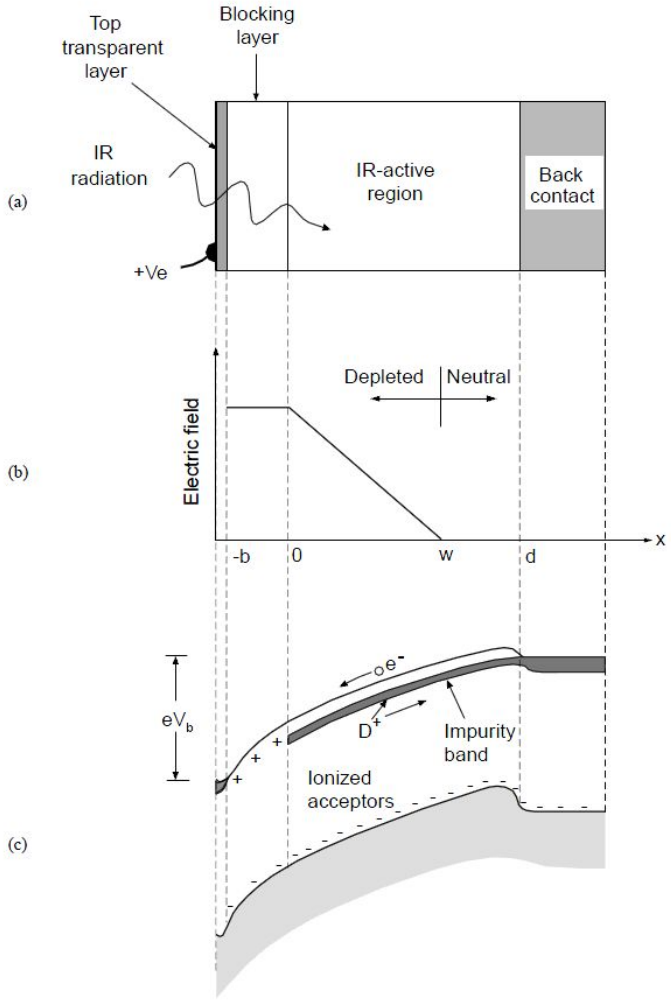

Figure 4.5.: Blocked impurity band detector (BIB): (a) cross section, (b) electric field, and (c) energy band diagram of the positively biased detector (taken from [38]).

The active layer is sandwiched between a degenerated substrate electrode and an undoped blocking layer. The photoexcitation of electrons takes place between the donor impurity and the conduction band. In the absence of an applied bias voltage, the charge neutrality requires equal

concentration of ionized donors. Negative charges are fixed at the acceptor sites and the ionized donors (D^+ charges) are mobile and can propagate through the active region via hopping between occupied (D^0) and vacant (D^+) neighboring sites. An electric field through a positive bias drives D^+ charges towards the substrate, while the undoped blocking layer prevents the injection of new D^+ charges. A depletion region, with a field dependent width of D^+ charges is created. This ionized - impurity depletion region is the active part of the detector. Photoionization of a neutral impurity in the depletion region generates a hole and an ionized impurity, which are swept in opposite directions by the electric field. Dark current from impurity band conduction is not present due to the blocking layer.

4.3.2. Fourier transform infrared spectrometer

A major task on spectroscopy is to characterize the spectrum of a light source. The instrument used to obtain the spectrum of the QCLs was a Bruker Vertex 80 fourier transform infrared spectrometer (FTIR). In principle FTIR spectroscopy is based on a Michelson interferometer (Fig. 4.6). Light from a source is split into two beams by a beamsplitter. In the two beam paths, one beam is reflected on a fixed and the other one on a movable mirror which introduces a time delay. The reflected beams interfere at the beam splitter and build the output signal on the detector. Measurements of the output signal taken on many discrete positions of the moving mirror build an interferogram, which shows the detected light over the mirror position. The spectrum can be reconstructed with fourier transformation of the recorded interferogram.
In this work the FTIR is used for the spectral measurements and has a maximum resolution of 0.075 cm^{-1}, which corresponds to 2.25 GHz. The beamsplitter in the Bruker FTIR is made of mylar.

For measurements, the internal DTGS (Deuterated Triglycine Sulfate) detector of the spectrometer was used. The room temperature operated DTGS-detector is a pyroelectric detector. Pyroelectricity is the spontaneous electric polarization in the material to temperature changes. A pyroelectric crystal between two electrodes is treated to absorb the incident THz radiation, if the electrode is transparent in the desired spectral region. Heat generated by this incident radiation raises the temperature of the crystal and induces a reduction of the spontaneous polarization and the surface charge simultaneously. Compared to other pyroelectric detectors, DTGS-detectors have a relatively high sensitivity at THz frequencies [1].

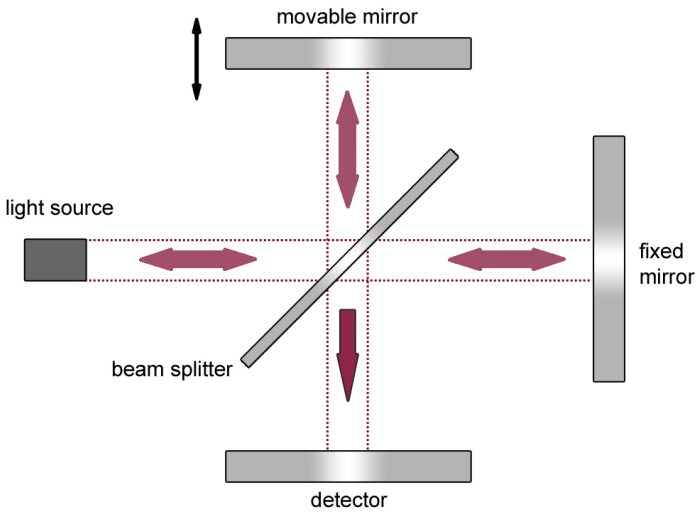

Figure 4.6.: Principle of a Fourier Transform Infrared Spectrometer based on Michelson Interferometer.

4.3.3. Integral THz - emission measurement setup 1D

The integral measurements for characterization of a QCL by the current versus voltage (I-V) or light versus current (L-I) plots were realized with the following setup (Fig. 4.7).

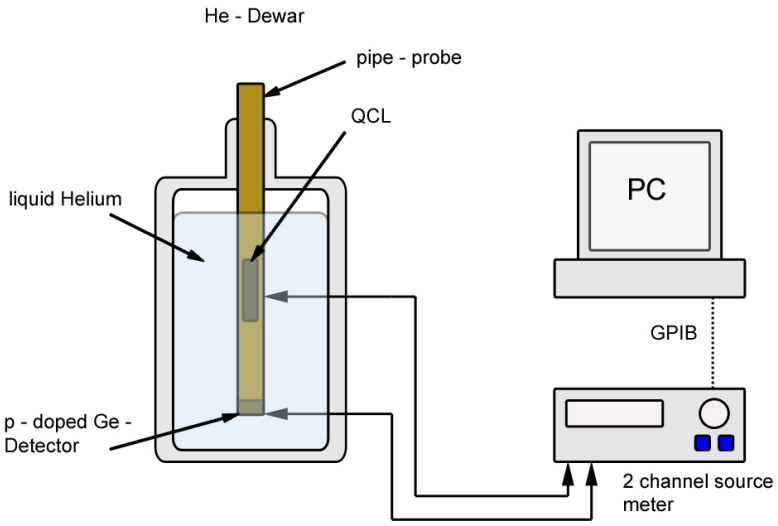

Figure 4.7.: Schematic of the setup for I-V measurements in liquid helium.

The QCL is mounted inside a pipe probe, which is inserted directly into a dewar filled with liquid helium (He). Due to the direct contact of the QCL and the liquid He, measurements at very low and stable temperatures at 4.2 K can be performed. The QCL sample is mounted on

one end of a lightpipe in the pipe probe, which guides the emitted radiation to the Ge-detector placed on the other side. The detector is biased with 2V DC from one channel of the Keithley 2612 source meter, which also records the current through the detector on the same channel. In channel two the voltage is ramped for the QCL and measures simultaneously the current through the device. The current dependent on the bias voltage of one QCL (I-V plot) and the received light on the detector (direct proportional to the measured current) through the sample current (L-I plot) is analyzed with a Keithley software and the described measurement setup.

4.3.4. Integral THz - emission measurement setup 2D

For the coupled integral THz - emission measurement basically the same setup is used as described above. The only difference is a second source meter, which is necessary to separately supply with voltage and measure the current from each of the two coupled QCLs (Fig. 4.8). One Keithley 2612 source bias the detector with 2V DC and measure the current dependent on the impinging THz radiation on the Ge-detector. Each channel of the second Keithley provides the bias voltage and current measurements to one segment of the coupled QCL. This setup was used to analyze the behavior of coupled QCL disk and ridge resonators. All components are also connected via a GPIB bus to a PC. The software, which recorded the measurement values, was programmed in Labview during this diploma thesis.

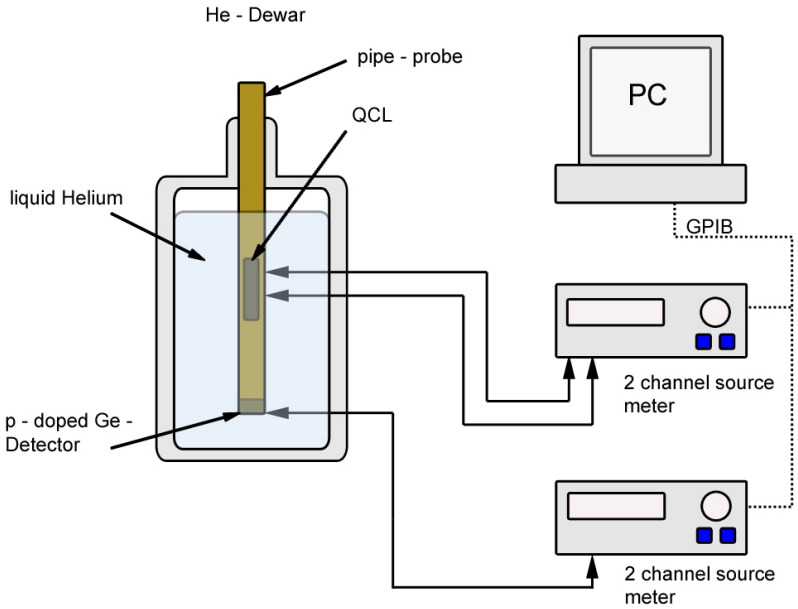

Figure 4.8.: Schematic of the setup for THz-emission measurements of coupled QCLs at liquid helium.

4.3.5. Spectral measurement setup

To analyze the spectral characteristics of single and coupled QCL devices, the illustrated setup in Figure 4.9 was used. The measurements are performed at cryogenic temperatures and controlled over a temperature controller connected to the cryostat. This is a chamber, which is evacuated to approximately 2×10^{-6} mbar during the measurement. The coldfinger of the cryostat, which is a liquid helium cooled copper plate, acts as a mounting device for the samples. The temperature is adjustable over the helium flux of the coldfinger. To couple out the emitted light of the cryostat a copolymer polymethylpentene (TPX) window is used. This polymer material is transparent for THz frequencies as well as in the visible and the absorption coefficient is less than 0.5 cm^{-1} at 1 THz. Its THz refractive index is 1.457 [1].

The outcoupled emission is collected by an off-axis parabolic mirror and enters the Fourier-transform spectrometer. The colinear beam is guided through the FTIR and focused on the internal DTGS-detector. Due to the strong water absorption of terahertz radiation the FTIR is purged with dry air during the measurements. The source meter delivers the bias voltage for single and coupled QCLs. For these measurements the delivered Bruker Vertex 80 software was used to record the spectra of the samples.

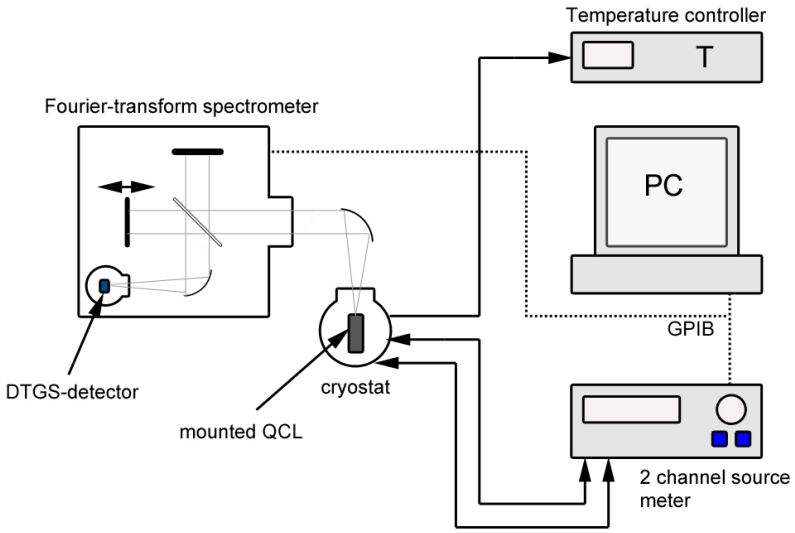

Figure 4.9.: Schematic of the setup for spectral measurements with the Fourier-transform spectrometer.

5. Experimental results

The current versus voltage (I-V), light versus current (L-I) characteristics and the field dependent spectra were recorded in continuous-wave mode operation. I-V and L-I measurements were performed with the setup described in Chapter 4.3.3 at liquid helium temperature of 4.2 K. The spectra of the different devices were recorded at a temperature of 7.5 K with the measurement setup shown in Chapter 4.3.5. The measurement for coupled disks and coupled ridges was recorded in continuous-wave (cw) mode operation at liquid helium temperature of 4.2 K with the setup described in Chapter 4.3.4.

5.1. Single disks

The electrical characterization of a single disk with a radius of R = 44 μm is shown in Figure 5.1. The measurement was performed with a continuously ramped bias voltage from 0 V to 20 V. Lasing of this single disk starts at a threshold current density J_{th} of 181 A/cm^2 with an applied voltage of 12.5 V (7.8 kV/cm). As the light intensity starts rising at J_{th}, the I-V shows a typical photon kink. At this point the photon assisted tunneling starts which increases the current. The region of negative differential resistance (NDR) is reached at a voltage of 13.17 V corresponding to an electric field of 8.23 kV/cm. Before the curve enters the NDR region, the maximum current density J_{max} of 220.2 A/cm^2 is transported through the device.
The estimated laser emission at 7.8 kV/cm from the bandstructure calculations (Fig. 2.8) is in good agreement with the measured device. Above 8.23 kV/cm either injection or extraction for depopulation breaks down and causes a misalignment of the bandstructure.

The threshold current density J_{th} does not show a significant deviation for disks with other dimensions (Table 5.1). The slight difference in the order of a few A/cm^2 results probably in consequence of the processing imperfections and the wire bonding process of the samples. For a couple of samples occurs a problem during the bonding process of the gold wire on the top gold contact. If the bonder settings are not perfectly chosen, the top gold layer near the bonding

wire is sometimes slightly removed. Another problem was to bond exactly central on top of the disk on such small devices.

The maximum current density J_{max} for all other measured disk radii is in the order of 240 - 270 A/cm^2 and significantly higher, compared to the disk with a radius of 44 μm. The lasing domain, which is between the photon kink at the threshold current density J_{th} and the kink before the NDR regime, increases with bigger disk radii. Measurements show the longest lasing domain for disks with R = 60 μm and the smallest for R = 44 μm.

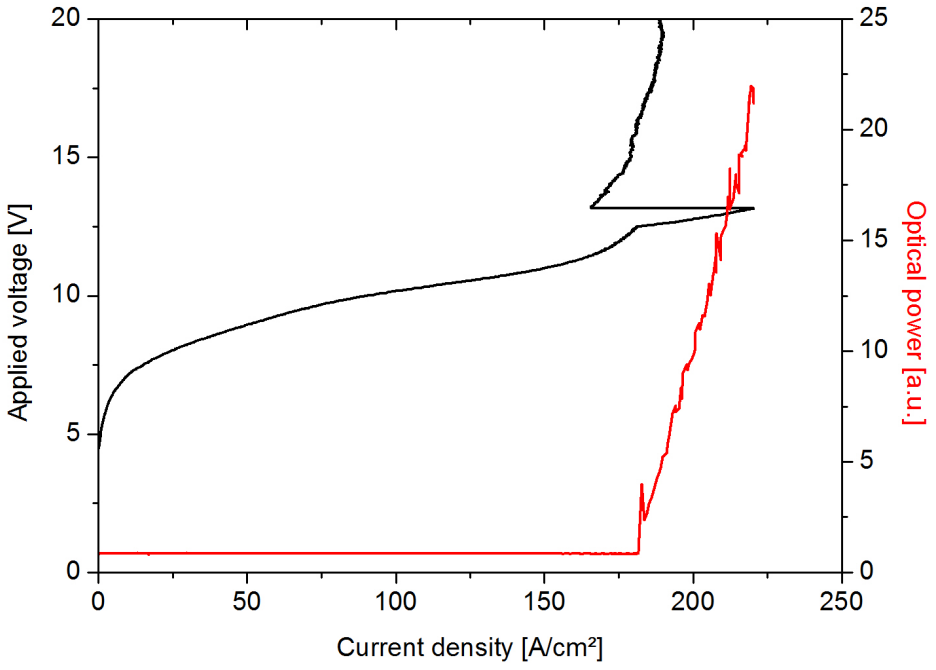

Figure 5.1.: Sample H256, single disk with radius R = 44 μm. I-V and L-I characteristics recorded in continuous mode. The threshold current density is 181 A/cm^2 at 12.5 V.

R [μm]	J_{th} [A/cm^2] (Bias [V])	J_{max} [A/cm^2] (Bias [V])	f near J_{max} [THz]	Modes
44	181.6 (12.5)	220.2 (13.17)	2.34	1
48.5	179.7 (12.07)	242.2 (13)	2.11	1
49	178 (12.06)	236.9 (12.86)	2.09	1
52.5	181.6 (12.1)	262.3 (13.2)	2.26	1
53.5	179.1 (12.08)	241 (13)	2.22	1
56	183.1 (12.05)	259.6 (13.3)	2.4	1
57	180 (12.07)	253 (13.23)	2.36	1
59.5	185 (12.16)	247 (13.28)	2.25; 2.2	2
60	185.2 (12.1)	262 (13.16)	2.24	1

Table 5.1.: Characteristics for all measured single disks.

Figure 5.2 shows the spectra at different bias points in the lasing domain for a disk with radius R = 44 μm. With this disk radius, the device has only one lasing mode for all bias points. This is also the case for the majority of all other measured devices with different disk radii. The spectra for R = 51.5 μm, R = 56 μm and R = 57 μm shows lasing starting in single-mode (SM), which jumps to another single-mode for higher bias voltages (see Fig. 5.3).

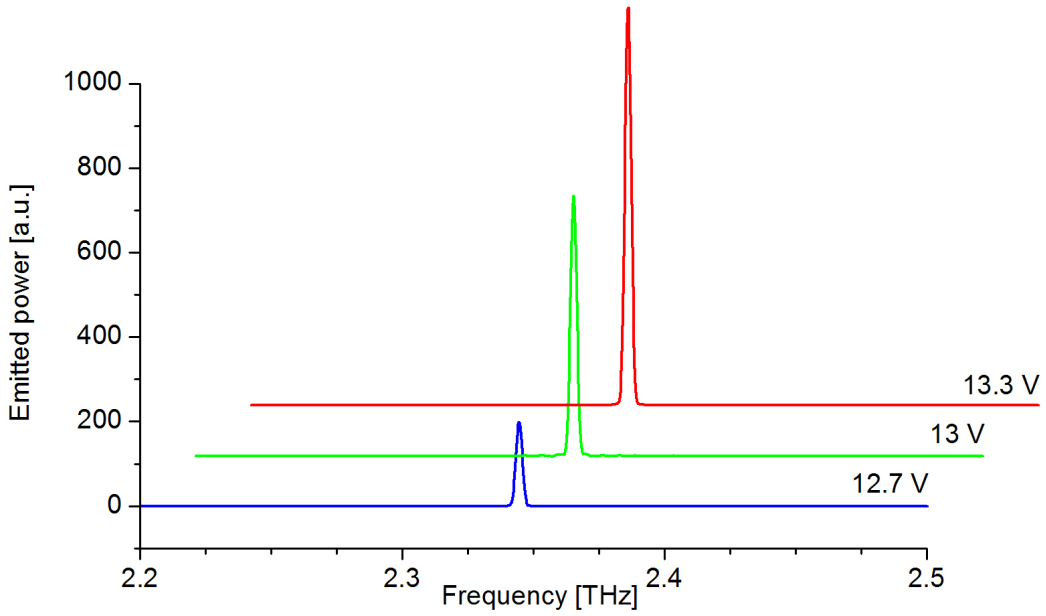

Figure 5.2.: Recorded spectra of a disk with radius R = 44 μm. The lasing frequency is constant at 2.34 THz with different bias voltages in the lasing domain.

Also multi-mode (MM) lasing occurs at a disk radius of R = 48 μm and R = 59.5 μm. In this case lasing starts single-mode for a small bias in the lasing domain and splits to multi-modes with increasing bias voltages (see Fig. 5.4).

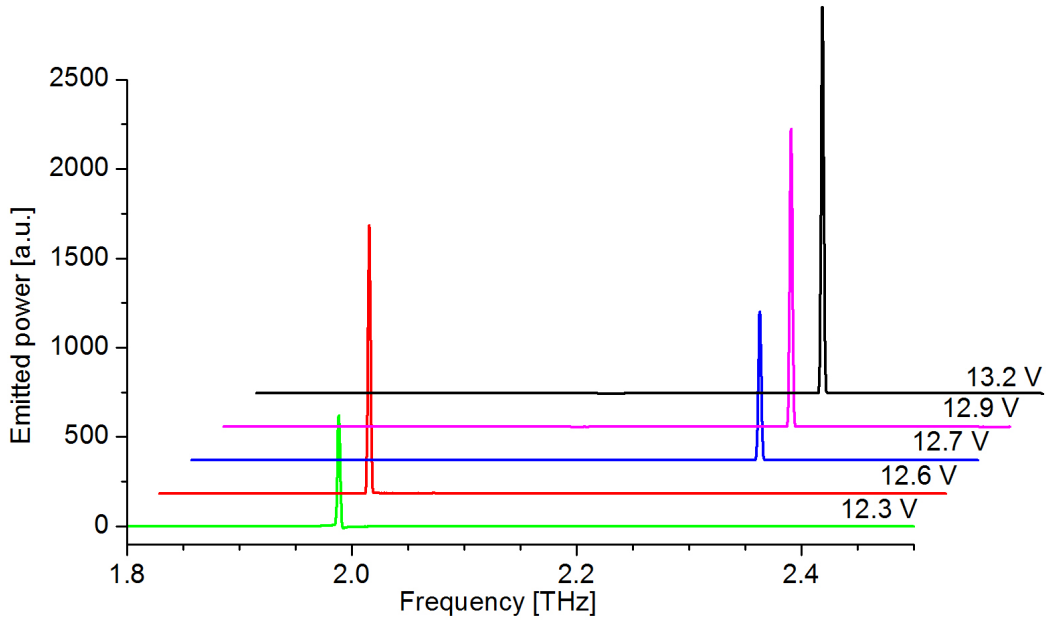

Figure 5.3.: Recorded spectra of a disk with radius R = 51.5 μm. The lasing frequency jumps from 1.98 THz to 2.3 THz for increasing the bias voltages in the lasing domain.

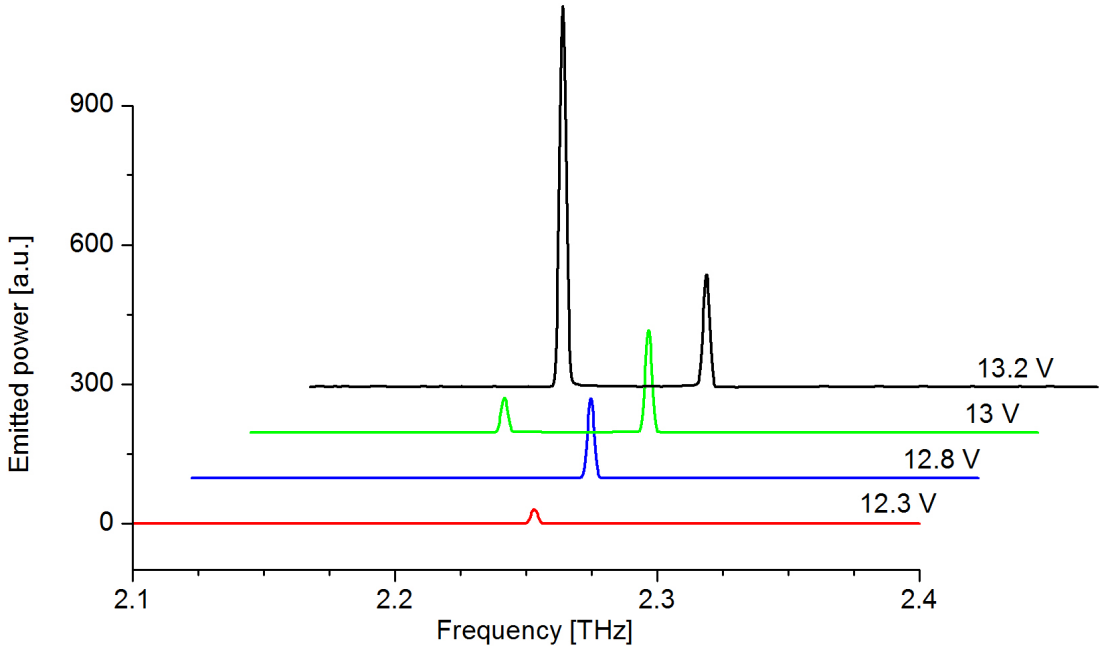

Figure 5.4.: Spectra of a disk with radius R = 59.5 μm, which starts lasing single-mode at 2.25 THz and splits to multi-mode lasing also at 2.19 THz inside the lasing domain.

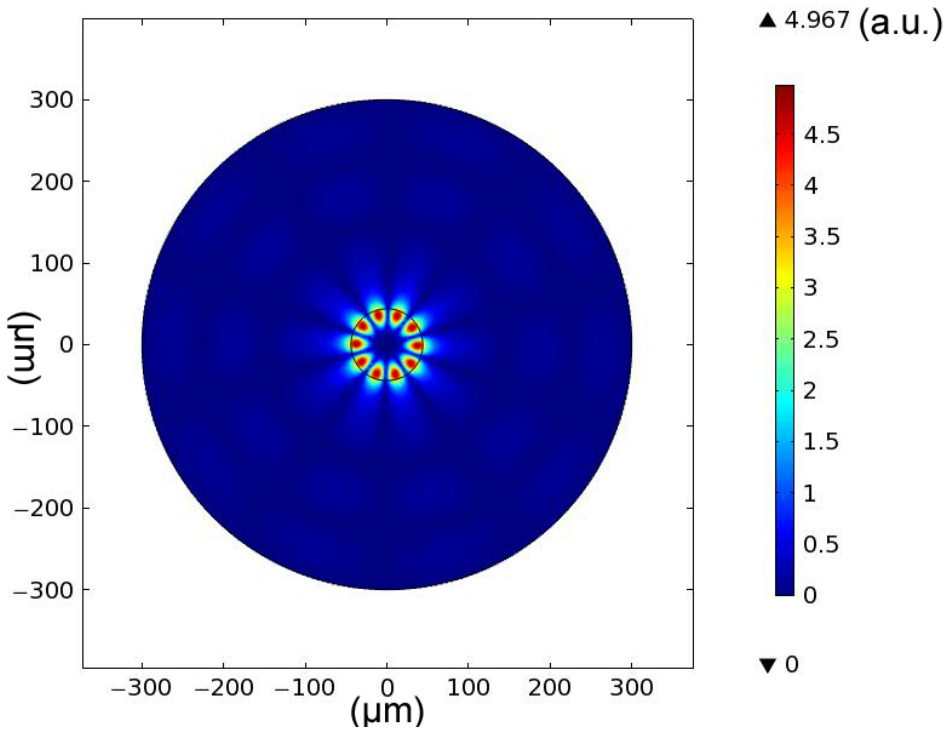

Figure 5.5.: Simulated whispering gallery mode (mode number m = 5) of a disk with radius R = 44 μm (effective refractive index $n_{eff} = 3.6$) surrounded with air. The corresponding frequency for this configuration is 2.27 THz.

To compare the measurement, all different used disk sizes were simulated with Comsol. Figure 5.5 shows the spatial field distribution of the z-component of the electric field from a disk with R = 44 μm. The comparison of the measured disks with the simulated ones are shown in Figure 5.6. Only the whispering gallery modes were used from the simulation (effective refractive index $n_{eff} = 3.6$) with the mode number m and the corresponding Eigenfrequency. The measured lasing frequencies fitted very well to the simulation values. The small deviations are probably from the disk sizes of the measured samples. Through small lateral under etching of the disk sidewalls during the processing, the disk sizes are little smaller compared to the size on the lithography mask. This fact would shift the measured points in Figure 5.6 slightly to the left, which yields to a better fitting of the simulated curve.

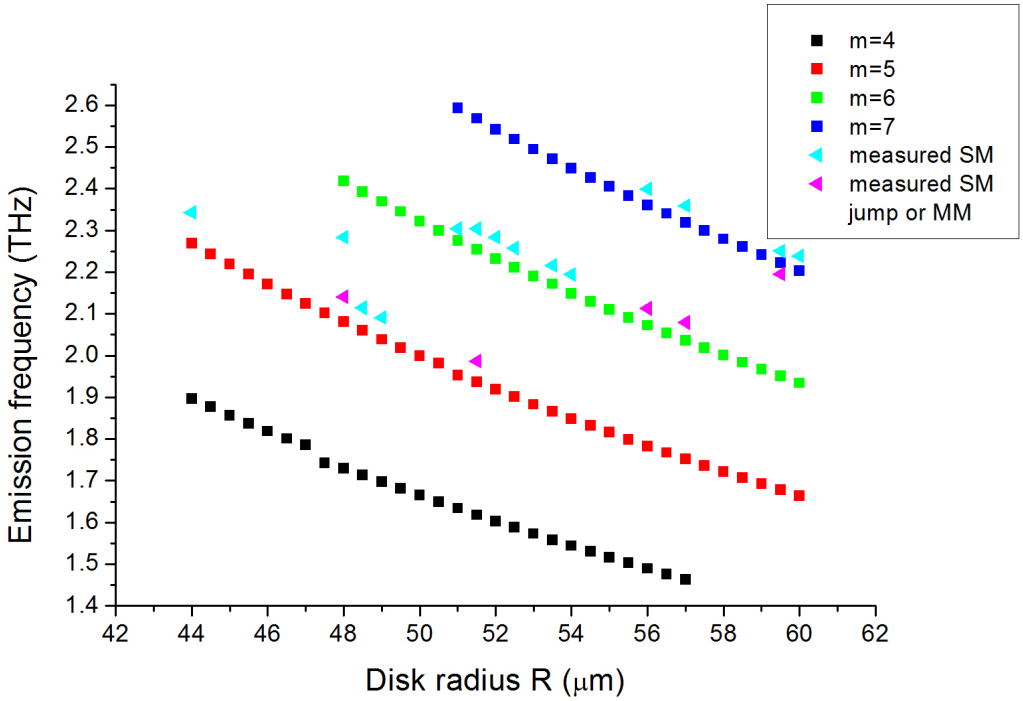

Figure 5.6.: Measured versus simulated emission frequency dependent on different disk radius.

5.2. Coupled QCL disk resonators

Coupled QCL disk measurements were performed to scale the influence of two independently biased disks located close to each other. For these measurements, each of the two disks was biased with a continuous ramped voltage from 0 V to 16 V with a step size of 0.1 V, and the emitted radiation was recorded over the photo current from the biased detector. The 2D-plots were created in such a way, that the disk with R_1 (vertical axis) was continuously biased from 0 V to 16 V and afterwards increased the bias voltage with the step size of 0.1 V of the disk R_2 (horizontal axis) and ramped again R_1 on the new bias voltage. To compare the results of the independently biased coupled QCL disks, also I-V and L-I measurements from each of the two disks were performed. Two different configurations were measured for the coupled QCL disk resonators with a gap of 4 μm and 6 μm and the disk radii were varied 47 μm, 50 μm, 52 μm and 54 μm. Fasching et al. [40] made similar measurements of coupled QCL disks with symmetric radii sizes, but these also called photonic molecules (PMs) were measured in pulsed mode operation with 100 ns short pulses and a duty cycle of 50 %. The difference to continuous mode operation, as used in this thesis, is that the measured values are integrated over several pulses and these mean values were recorded.

Coupled disks: $R_1 = 50$ μm, $R_2 = 50$ μm, gap: 4 μm

Figure 5.7 shows the result of two coupled disks with radius $R_1 = 50$ μm and $R_2 = 50$ μm with a distance between the disks of 4 μm. Disk R_1 starts to lase at a threshold current density J_{th} = 184 A/cm^2 (12.6 V) and has the maximum current J_{max} = 206 A/cm^2 at a bias voltage of 13.1 V, when the second disk R_2 has no bias voltage. The second disk R_2 starts lasing at J_{th} = 186 A/cm^2 (12.7 V) and has J_{max} = 209 A/cm^2 at a bias voltage of 13.2 V with the first disk R_1 without bias. Both QCL disks lase independently, i.e. when the second disk is not pumped. If both disks are supplied with different bias voltages, there is a "crosstalk" between disk R_1 and R_2. Disk R_1 stops lasing, when the bias voltage of disk R_2 is between 6.3 V and 9 V. The same situation appears for disk R_2 with R_1 is between 3 V and 7.9 V. The maximum emission of both disks appears at the intersection of the bias voltages at 13.1 V with the corresponding current densities J = 240 A/cm^2 in disk R_1 and J = 250 A/cm^2 in disk R_2. Near this crossing point, the threshold current densities J_{th} decreases in the order of 20 A/cm^2 for both disks.
Martl et. al [41] shows the spectral gain and losses through modulation experiments of the H256 material system, which is the same as used in this thesis. In Figure 5.8 this gain/loss curve is

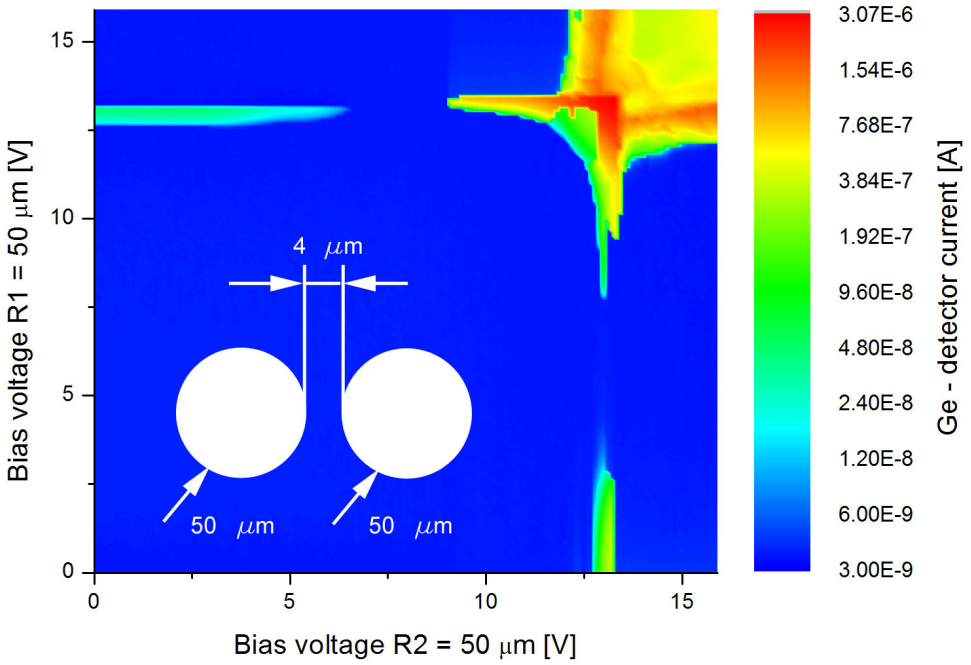

Figure 5.7.: Coupled disks with a gap of 4 μm between the disks and $R_1 = 50$ μm and $R_2 = 50$ μm.

compared with the output power of disk R_1 at 13.1 V and different bias voltages of disk R_2. This explains the on-off lasing behavior of disk R_1 dependent on different bias voltages of R_2. Both disks lase independently, when the second disk is not pumped. But if the second disk is biased between 5 V and 10 V, the disk acts as a tunable absorber because of the alignment of intersubband levels with loss for disk R_1 and has the possibility to suppress lasing due to the increase in losses for the coupled system. In this region affects the coupling awfully well to disk R_2, because the single peak gain of R_1 is not enough to compensate the increased losses. The coupling in this configuration with both disk radii of 50 μm and a gap of 4 μm is strong enough to switch lasing on-off in each of the disks with the other one. This unique possibility to control the gain and loss of each disk cavity externally, allows the controlling of the lasing emission.

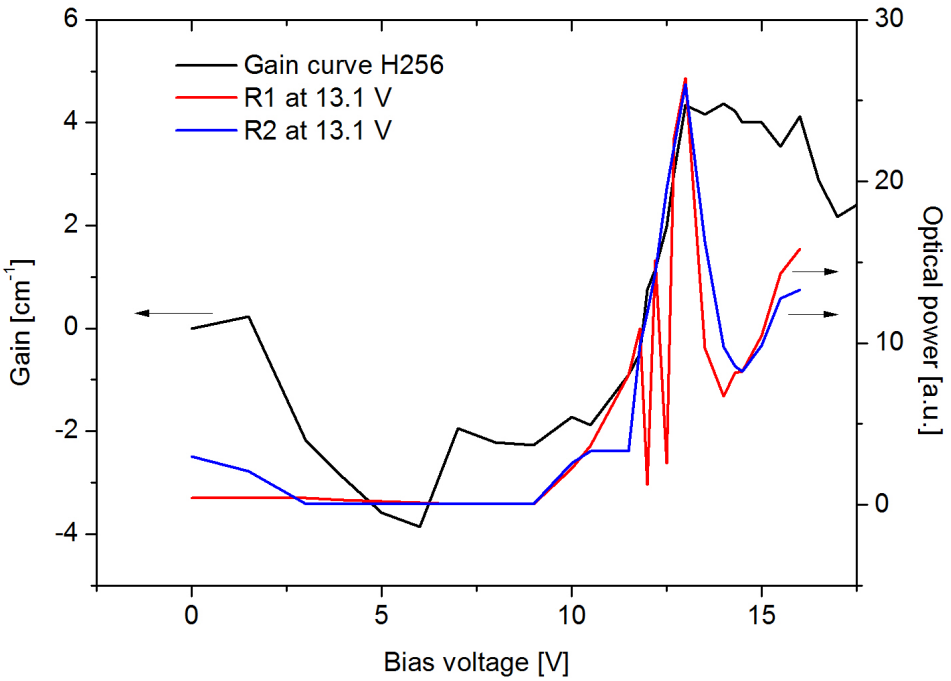

Figure 5.8.: Gain curve of H256 material system [41] compared with the optical output power of disk R_1 and R_2 at 13.1 V and different bias voltages of the other disk.

Coupled disks: $R_1 = 52\ \mu m$, $R_2 = 52\ \mu m$, **gap:** $4\ \mu m$

The measurement of a sample with a gap of 4 μm and equal disk radii of the two disks with $R_1 = R_2 = 52\ \mu m$ is shown in Figure 5.9. Both disks do not lase independently and only emit THz radiation at the intersection of both lasing domains, where both cavities provide gain. The corresponding current densities in the maximum of the emitted radiation on the Ge - detector are for disk R_1 at 13.1 V ($J_{max} = 223$ A/cm^2) and for disk R_2 at 13 V ($J_{max} = 213$ A/cm^2). The threshold current densities J_{th} for both disks decrease by about 8 A/cm^2 near the NDR regime inside the lasing domain. This is a consequence of the strong intercavity coupling and results in the triangular shaped emission pattern in the 2D plot.

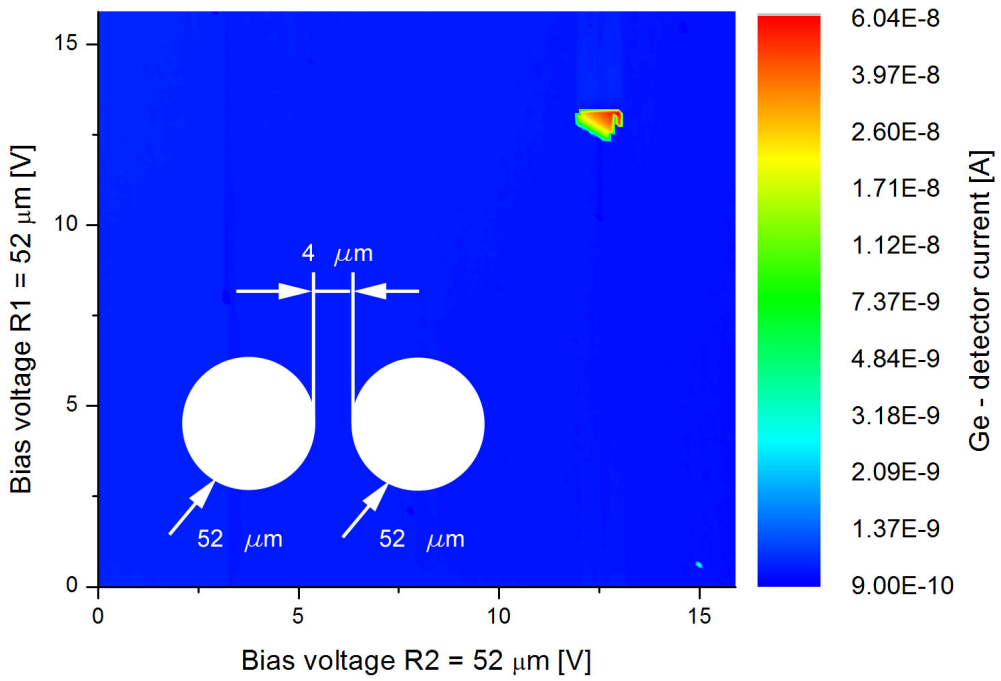

Figure 5.9.: Coupled disks with a gap of 4 μm between the disks and $R_1 = 52$ μm and $R_2 = 52$ μm.

Coupled disks: $R_1 = 50$ μm, $R_2 = 47$ μm, gap: 4 μm

The independent recorded I-V and L-I measurements of this configuration are shown in Figure 5.10. The lasing domain of disk R_1 starts from 12.3 V ($J_{th} = 176$ A/cm^2) and ends before the I-V turns into the NDR regime at 13 V with a current density $J_{max} = 221$ A/cm^2. The I-V for the second disk R_2 has the same shape, but with different threshold ($J_{th} = 182$ A/cm^2) and maximum current density $J_{max} = 233$ A/cm^2 is transported through the device. The emitted optical power of disk R_2 is much higher compared to disk R_1. An explanation for this difference might be, that the possible mode for this cavity fits better to the gain maximum and therefore reaching a higher output power. Moreover this effect might be enhanced due to a non linearity behavior of the Ge - detector. Due to these different power levels of both disks, the 2D coupling plot is asymmetric.

The 2D plot of the described independent lasing QCLs is shown in Figure 5.11. This configuration shows a similar behavior which is seen for the disks with equal radii $R_1 = R_2 = 50$ μm and the same gap size. With different dimensions for the cavities, one disk cannot completely switch off the second disk, but an influence is noticeable on the dynamic range. First of all, the

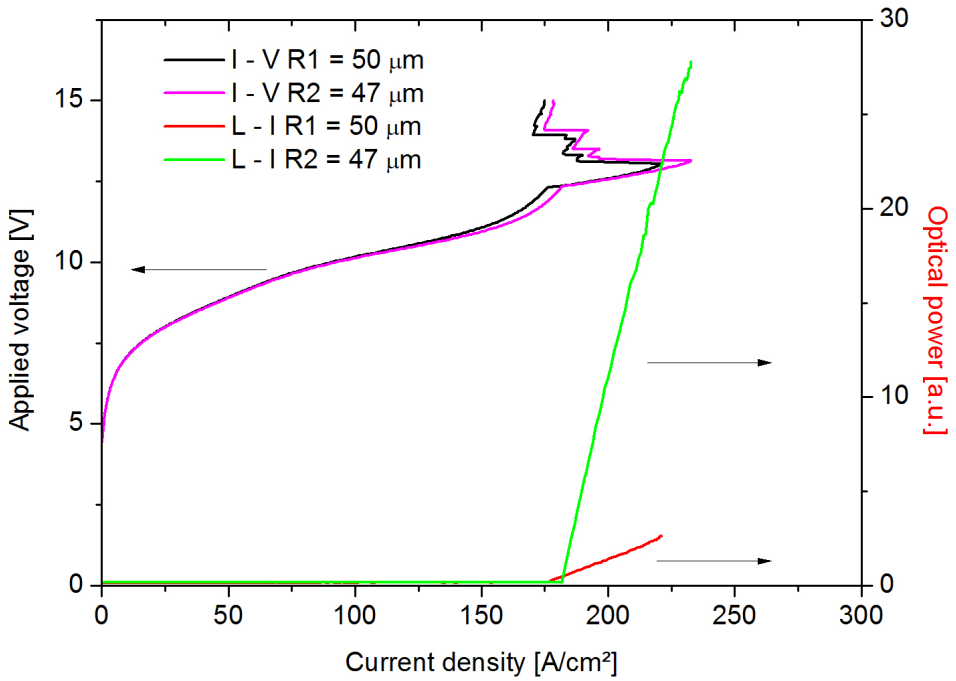

Figure 5.10.: Independent recorded I - V and L - I from the disk $R_1 = 50\ \mu m$ and $R_2 = 47\ \mu m$ with a gap of 4 μm between the disks.

emitted optical power of the disks, which is equivalent to the Ge - detector current, is different in one order of magnitude.

The region of influence is pretty much the same between 5 V and 10 V for both disks as for the $R_1 = R_2 = 50\ \mu m$ sample. The disk R_1 shows a pretty constant radiation at a bias voltage between 12.4 V and 13.4 V with a lower emitted output power compared to disk R_2. The lasing domain of disk R_2 is slightly broader and with a higher emitted output power. The possible influence from one disk to the lasing domain of the other disk affects in a slight increase of the threshold current J_{th} and a narrower domain width between 5 V and 10 V. As noticed before, the influence at different disk sizes is not enough to completely discard the radiation of the second disk, but strong enough to affect the characteristic in the high loss region.

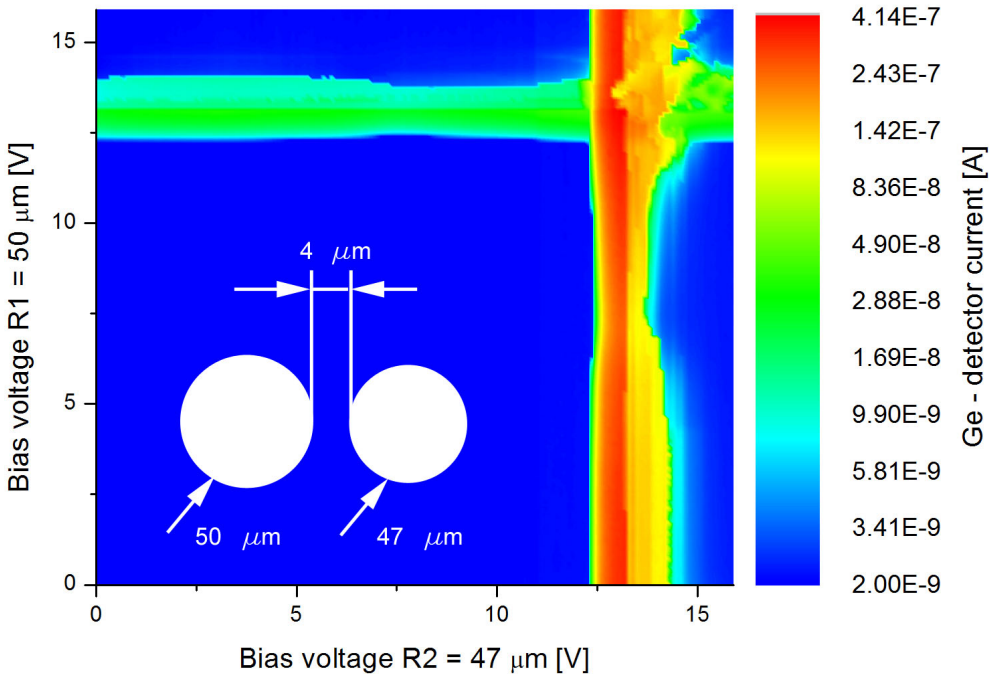

Figure 5.11.: Coupled disks with a gap of 4 μm between the disks and $R_1 = 50$ μm and $R_2 = 47$ μm.

Coupled disks: $R_1 = 52$ μm, $R_2 = 52$ μm, gap: 6 μm

The coupled disk with $R_1 = R_2 = 52$ μm and a gap of 6 μm between the disks shows the same coupling behavior (Fig. 5.12) compared to the disks with the same dimensions and a 4 μm gap (Fig. 5.9). Independent lasing is not possible which indicates the strongest coupling with the triangular shaped emission pattern also in the case of a 6 μm gap and same disk sizes. Compared with the smaller gap of 4 μm, the coupling influence is weaker, because the combined lasing domain is broader and therefore lasing occurs for smaller bias voltages. This means, that the single peak gain of one cavity is larger for smaller bias voltages than the loss of the coupled system.

This configuration only emits THz radiation at the intersection of the lasing domains from both disks. The corresponding values at the maximum, before the NDR region starts, are at a bias voltage of 13 V with the maximum current densities through the devices $J_{max} = 235$ A/cm^2 for both disks. The lowest threshold current density combinations are $J_{th} = 188$ A/cm^2 (12.8 V) for R_1 and $J_{th} = 180$ A/cm^2 (12.8 V) for R_2 and decreases for both disks of about 7 A/cm^2 near the NDR region inside the lasing domain. Compared to the sample with the 4 μm gap,

the recorded current in the Ge - detector equivalent to the emitted output power is by a factor 2 higher.

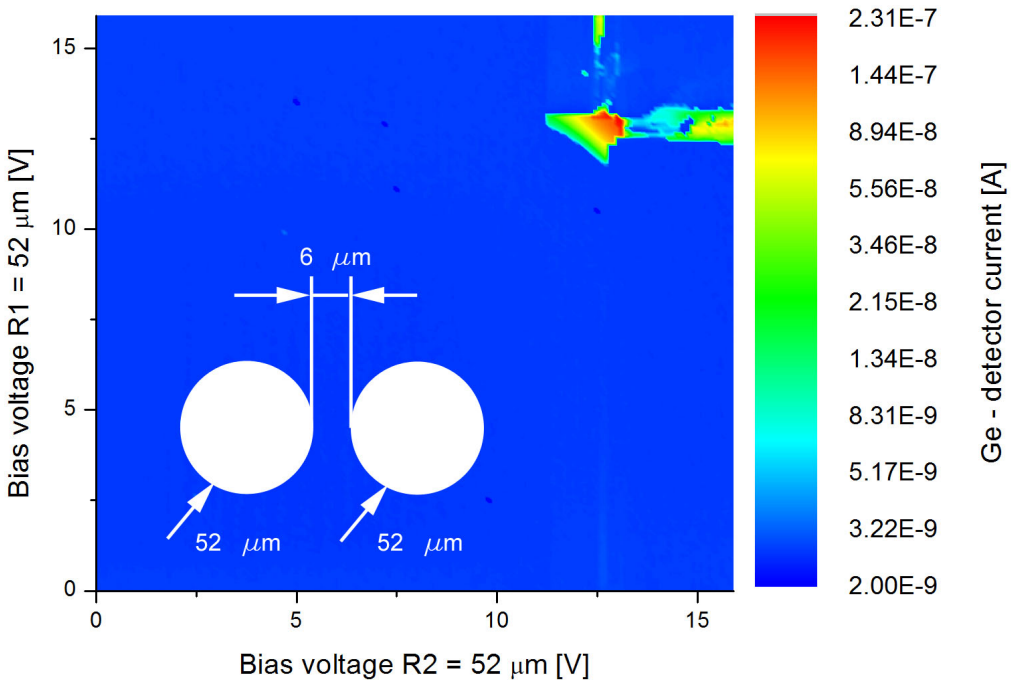

Figure 5.12.: Coupled disks with a gap of 6 μm between the disks and $R_1 = R_2 = 52$ μm.

Coupled disks: $R_1 = 52$ μm, $R_2 = 54$ μm, gap: 6 μm

Different disk sizes with a gap of 6 μm allow the disks to lase independently. This requires, that the loss of the coupled system is not enough to prevent one disk of emitting THz radiation, even if the second disk is in the high loss region. The influence of the bias voltages from one disk to the lasing behavior is shown in Figure 5.13.

Disk R_1 has a threshold current density J_{th} of 184.6 A/cm^2 (12.2 V) and a maximum density of $J_{max} = 252$ A/cm^2 (13.1 V) before the NDR regime starts, if the second disk is unbiased. Compared to the same disk size with a 4 μm gap, the threshold is equal, but the maximum current through the device is higher and differs of 17 A/cm^2. The corresponding current densities for the second disk R_2 in the coupled system are $J_{th} = 183.4$ A/cm^2 (12.2 V) and $J_{max} = 244.4$ A/cm^2 (13 V). The 2D plot shows only a slight influence to the emission of one disk, when the second disk is in the loss regime between 5 V and 10 V. The asymmetric plot has the maximum optical power at the intersection region of both lasing domains at 13 V.

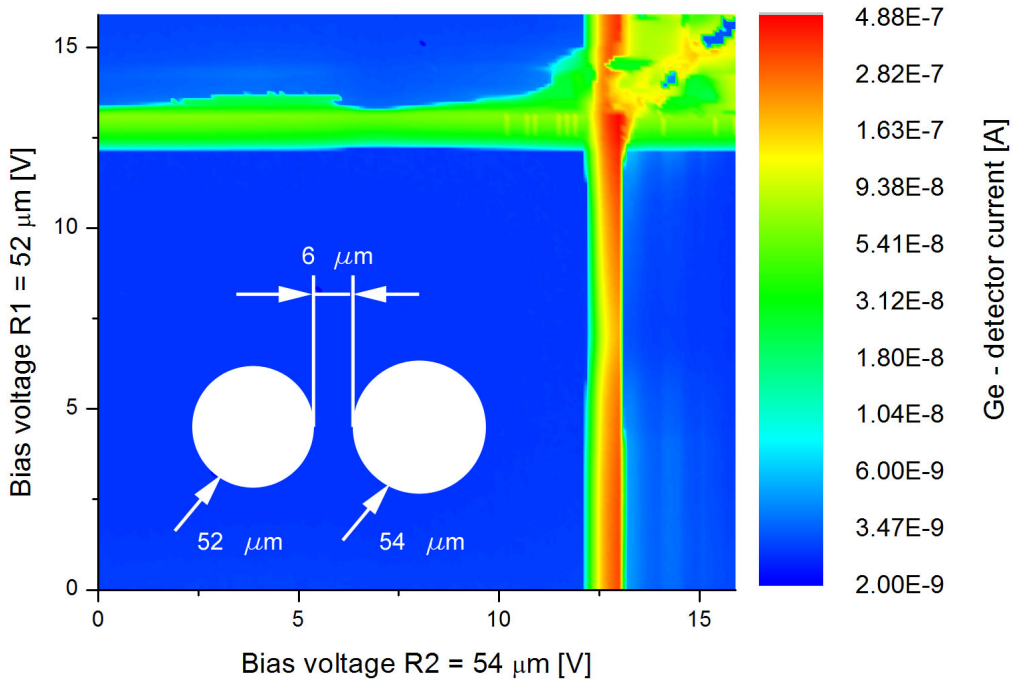

Figure 5.13.: Coupled disks with a gap of 6 μm between the disks and $R_1 = 52\ \mu m$ and $R_2 = 54\ \mu m$.

The measurements reveal, that strong optical intercavity coupling for small gap sizes (4 μm and 6 μm) depends on the disk sizes. For asymmetric configurations of the cavities, the disks of the coupled system lase independently and show only a slight influence in the high loss regions. A mode-mismatch of the different disk sizes leads to the weaker influence and less coupling of the disks. A symmetric coupled system with equal disk sizes has a stronger coupling behavior, which depends on the cavity dimension. The possibility to externally control the lasing emission over the bias voltage from the second disk in continuous mode operation shows only the sample with a gap of 4 μm and $R_1 = R_2 = 50\ \mu m$.

5.3. Coupled QCL ridge resonators

A second type of DM QCL resonators was built to analyze the coupling in DM waveguides. For this measurements, ridges with the two lengths (1 mm and 2.5 mm) and width (50 μm for all ridges), but with different gap sizes were processed. The width for the QCLS was chosen relatively narrow to ensure cw operation mode for the measurements. Different gap sizes were selected between 3 μm and 20 μm. For the small gaps lasing were expected only if both ridges were pumped, and for the huge gaps (20 μm) independent lasing was assumed. Switching behavior for radiation was predicted in between. The 2.5 mm long ridges were measured to reveal the effect of the longer absorption length for the coupled cavities.

Coupled ridges CR3 - L - 1: $L_1 = L_2 = L =$ **1 mm, gap: 3** μm

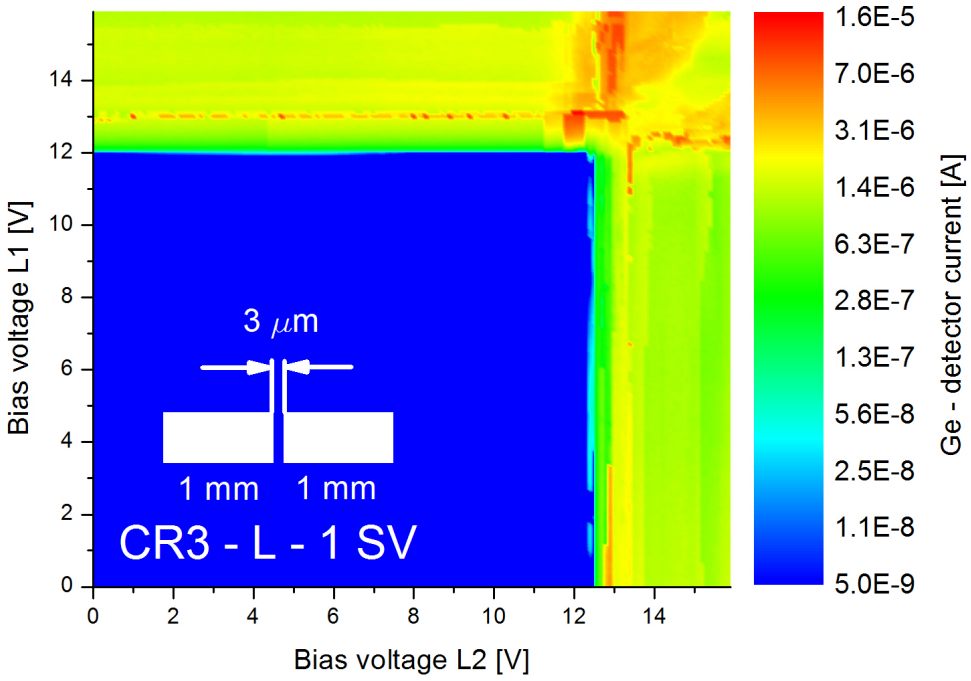

Figure 5.14.: CR3 - L - 1 SV: Coupled ridges with a gap of 3 μm between the two ridges of $L_1 = L_2 = L = 1$ mm and scanning in vertical (SV) direction.

Figure 5.14 shows the measurement of coupled ridges (CR) with a length of $L = 1$ mm and a gap between the facets of 3 μm (Coupled ridges CR3 - L - 1). This plot was created by continuously ramping the bias voltage in ridge L_1 and increasing the bias by a step size afterwards, from now on described as SV (scanning vertical). The maximum of the lasing emission of L_1 is not

constant and has different maxima at the Ge - detector, when the bias voltage is increased on the other ridge L_2. This behavior was reproducible also when the bias voltage was ramped manually, which excludes a failure in the Labview measurement program.

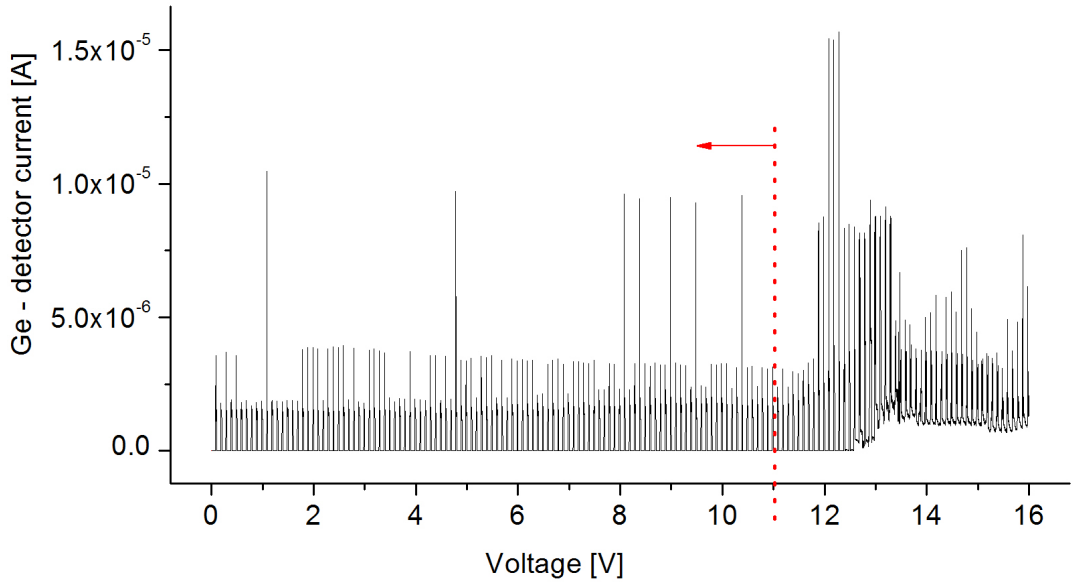

Figure 5.15.: All Ge - detector current values from CR3 - L - 1 in Figure 5.14

The plot in Figure 5.15 shows all the recorded Ge - detector current values from CR3 - L - 1 SV. There are mainly three different maximum current values before the bias voltage in the second ridge reaches the lasing domain. Spectral measurements of each ridge, with the second ridge unbiased, were recorded to analyze the reason for this deviation (Fig. 5.16). Between the measurements, the bias voltage is decreased to zero to obtain the same preconditions as for the measurements in the 2D plot. Lasing emission occurs at the bias voltage of 12.7 V, which is the maximum of the lasing domain before the NDR region starts, only in a single mode. The corresponding current density through the device is similar for all recorded spectra in the order of 255 A/cm^2. The measurement shows either a single mode at 2.16 THz or another one at 2.12 THz with a higher amplitude. The calculation of the mode spacing for a 1 mm ridge length with equation 2.30 from Chapter 2.3.3 results a mode spacing of 40 GHz with an effective refractive index of $n_{eff} = 3.6$, which is the same compared to the spectral measurement.

The explanation for the different current values of the Ge - detector may depend on the spectral

response of the detector. Another possibility is also the fitting of the mode with the gain curve of the active material. Therefore it is possible, that one mode creates a higher detector current compared to the other possible mode at a different frequency.

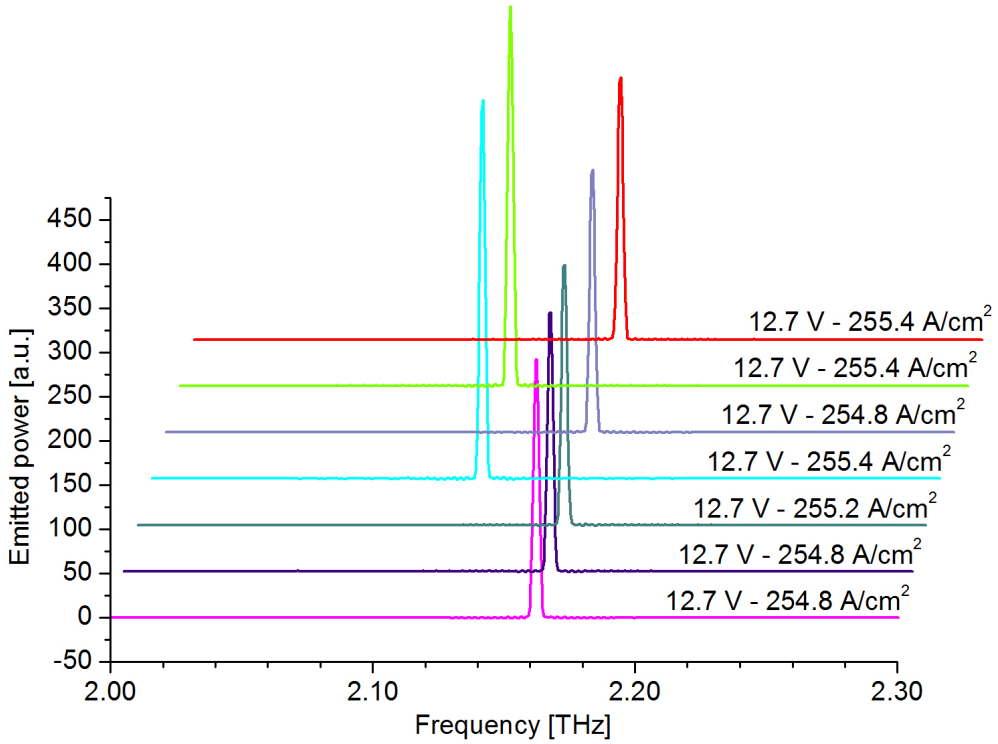

Figure 5.16.: Recorded spectra of one ridge from the configuration CR3 - L - 1.

The appearance of the two single modes is statistically arbitrary (Fig. 5.16). Each of the frequency dependent mode is possible near the gain maximum within the gain curve of the material system and only one mode appears, which is due "random" gain competition. The corresponding second ridge of the coupled configuration shows the same spectral behavior. It emits only single mode THz radiation at 2.12 THz or 2.16 THz with a bias voltage of 12.7 V and a current density of 255 A/cm^2 through the device. The statistical behavior, which of the two mode appears, is again completely arbitrary.

The dotted maxima of the Ge - detector current appears mainly in the scanning direction, because only in this direction is the ridge supplied from 0 V to 16 V for each bias voltage step of the second ridge. To compare both ridges of the coupled configuration, the measurements were also performed for the second ridge L_2 with a horizontally scanning (HS) direction to create the 2D plot (Fig. 5.17). Both ridges lase independently and show a weak dependency before the intersection of the lasing domains from L_1 and L_2. Near this point at a bias voltage of 12 V is a maximum of the emitted radiation for each ridge in scanning direction. When ridge L_1 and L_2

are in the lasing region at the crossing of both domains, the consequence of coupling is obvious. Some kind of mode competition between the two ridge resonators leads to a lower radiation of both QCL ridges compared to the emission of only one ridge. These effects are also evident in the NDR regions of the 2D plots, where lasing emission is still observed through forming electric field domains.

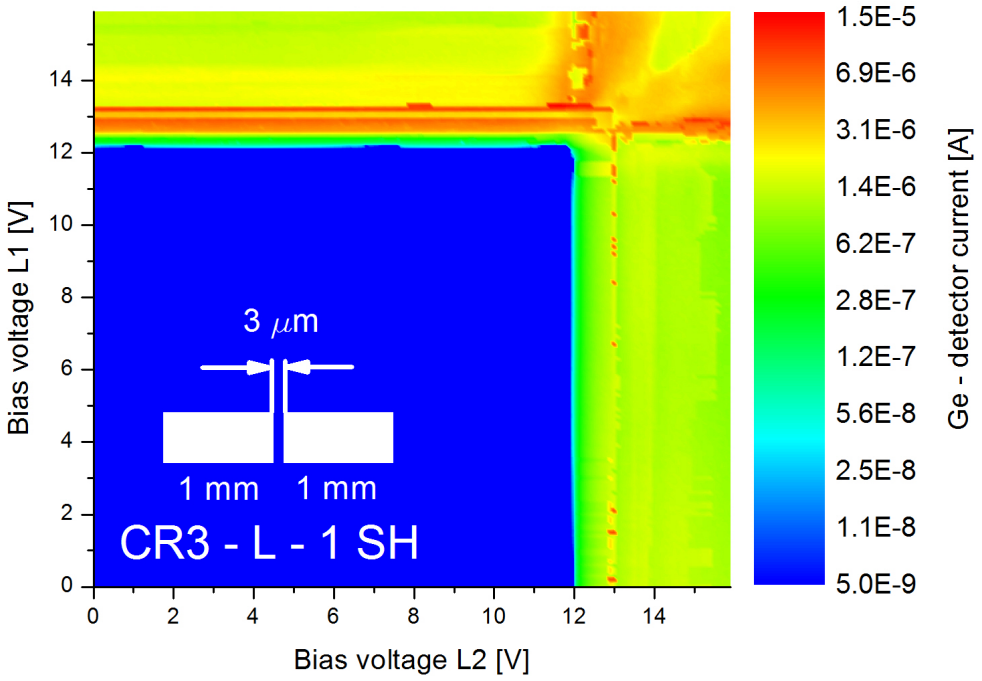

Figure 5.17.: CR3 - L - 1 SH: Coupled ridges with a gap of 3 μm between the two ridges of $L_1 = L_2 = L = 1$ mm and scanning in horizontal (SH) direction.

To confirm the assumption of coupling, two completely independent located ridges with $L_1 = L_2 = L = 2.5$ mm on a sample were recorded (Fig. 5.18). The plot shows both ridges lasing independently and a maximum of radiated transmission when both ridges are in the lasing domain before the NDR region.

Figure 5.19 shows the recorded spectra of $L_1 = L_2 = L = 1$ mm and a gap of 3 μm, when ridge L_1 is biased constantly with a voltage of 12.7 V and L_2 is supplied with different voltages. It occurs only a single mode at a frequency of 2.16 THz until ridge L_2 reaches its lasing domain. A voltage of 12.5 V at L_2 splits this mode into two close adjacent modes with frequencies of 2.16 THz and 2.166 THz. In the maximum of the domain from L_2 at 12.7 V appears two modes at a frequency of 2 THz and 2.166 THz.

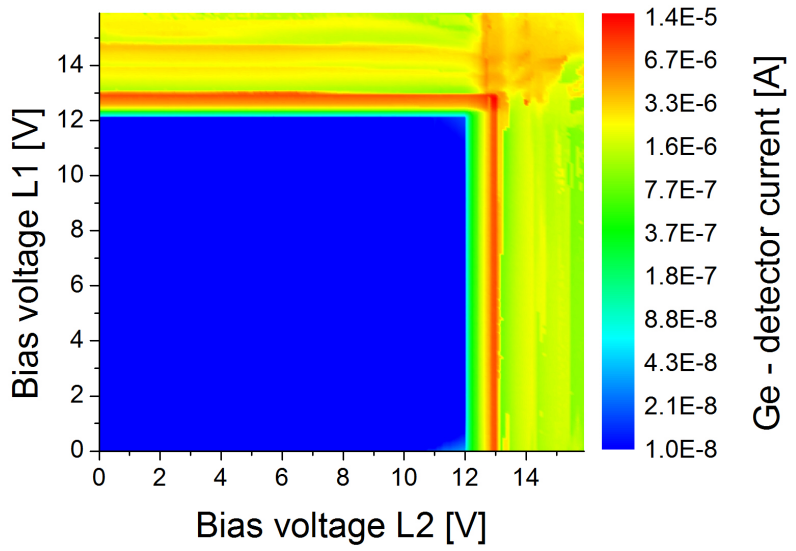

Figure 5.18.: 2D plot of completely uncoupled ridges with a ridge length of $L_1 = L_2 = L = 2.5$ mm.

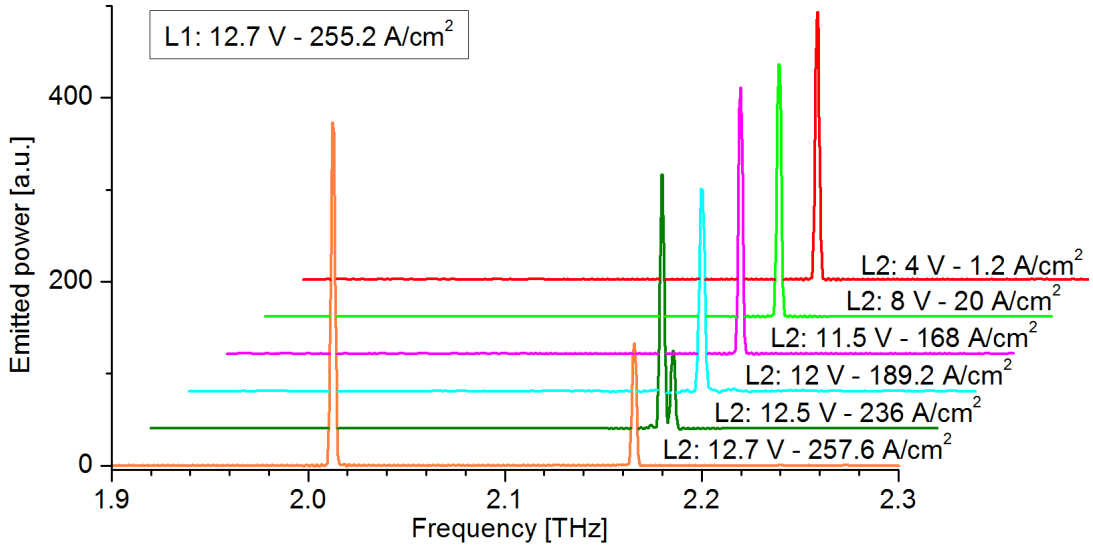

Figure 5.19.: Spectra CR3 - L - 1. Ridge L_1 is biased constantly with 12.7 V and recorded the spectra at different bias voltages of L_2.

Coupled ridges CR6 - L - 1: $L_1 = L_2 = 1$ mm, gap: 6 μm

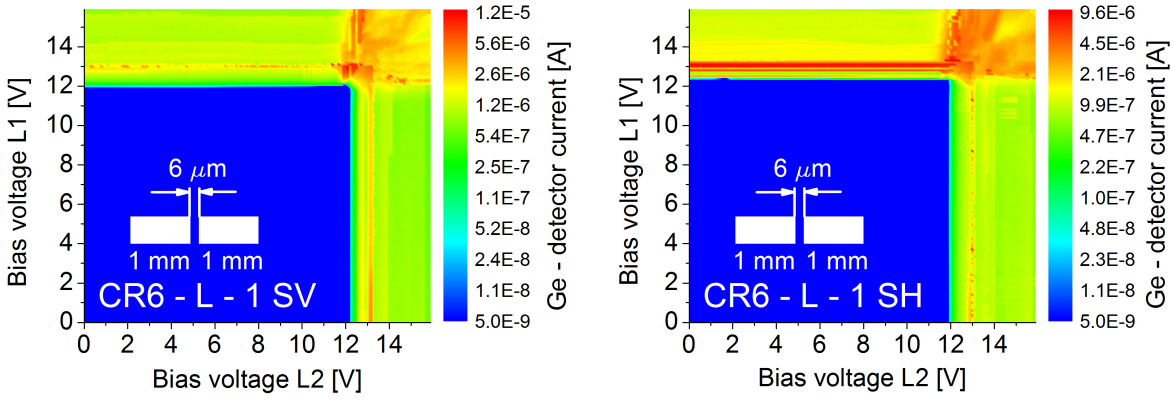

(a) CR6 - L - 1 SV (b) CR6 - L - 1 SH

Figure 5.20.: Coupled ridges CR6.

The SV (a) and SH (b) 2D plots of the coupled ridges with the dimensions $L_1 = L_2 = 1$ mm and a gap of 6 μm between are shown in Figure 5.20. The plots have a similar behavior compared to the case of CR3 - L - 1. Both ridges lase independently with a weak dependency before the intersection of the lasing domains. The maxima of the emitted radiation are again before the second ridge reaches its maximum.

Spectral measurements of the ridge L_1 shows two or three modes at 2.125 THz, 2.139 THz and 2.16 THz with a bias voltage of 13 V and the second ridge unbiased. L_2 has only one mode with a frequency of 2.09 THz at 13 V. It seems, that the gap size between the two ridges also affects the mode appearance of possible modes. Table 5.2 shows the threshold and maximum current densities of L_1 and L_2 for an unbiased second ridge.

Ridge	L [mm]	Gap size [μm]	J_{th} [A/cm^2] (Bias [V])	J_{max} [A/cm^2] (Bias [V])
L_1	1	6	188 (12)	264 (12.9)
L_2	1	6	188 (12)	267 (13)

Table 5.2.: Coupled ridges CR6

Coupled ridges CR10 - L - 1: $L_1 = L_2 = 1$ mm, gap: 10 μm

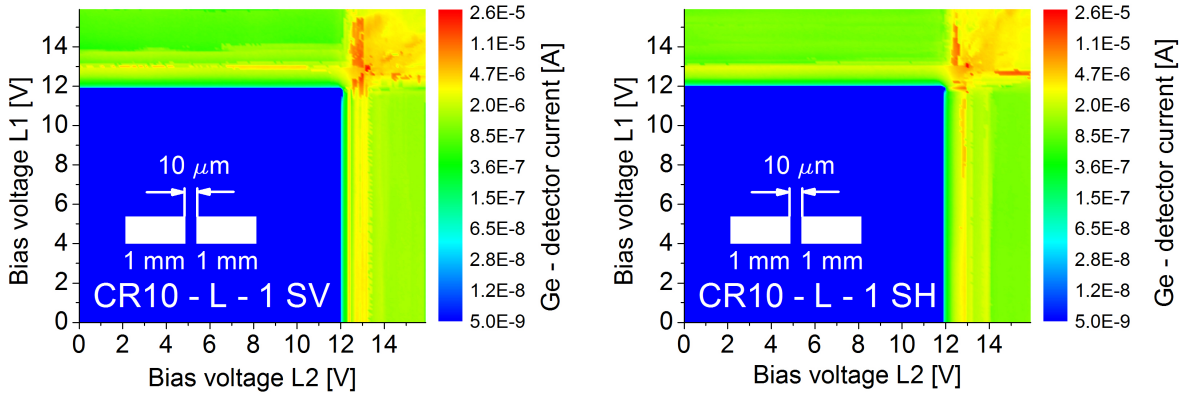

(a) CR10 - L - 1 SV

(b) CR10 - L - 1 SH

Figure 5.21.: Coupled ridges CR10.

Figure 5.21 shows the SV (a) and SH (b) recorded plots of coupled ridges with $L_1 = L_2 = 1$ mm and a gap of 10 μm. The measurements reveal independent lasing of both ridges. The maximum emitted THz radiation occurs on the Ge - detector, when both ridges are in their lasing domains. There is still a coupling effect, due to the fact that the emission maximum is not at the crossing points at 13 V of the bias voltages from L_1 and L_2. The maxima appears slightly before and after this specific point.

The spectral behavior of ridge L_1 and L_2 shows more possible modes with the increased gap size of 10 μm. The ridge L_1 has two or three possible modes with different combinations located at different frequencies of 2 THz, 2.09 THz, 2.13 THz and 2.16 THz. At the second ridge L_2 appears always two modes at 12.3 THz and 12.7 THz for the emitted radiation. The characteristic current densities through both devices are shown in Table 5.3.

Ridge	L [mm]	Gap size [μm]	J_{th} [A/cm^2] (Bias [V])	J_{max} [A/cm^2] (Bias [V])
L_1	1	10	188 (11.93)	272 (12.97)
L_2	1	10	189.6 (11.95)	271 (12.84)

Table 5.3.: Coupled ridges CR10

Coupled ridges CR20 - L - 1: $L_1 = L_2 = 1$ mm, gap: 20 μm

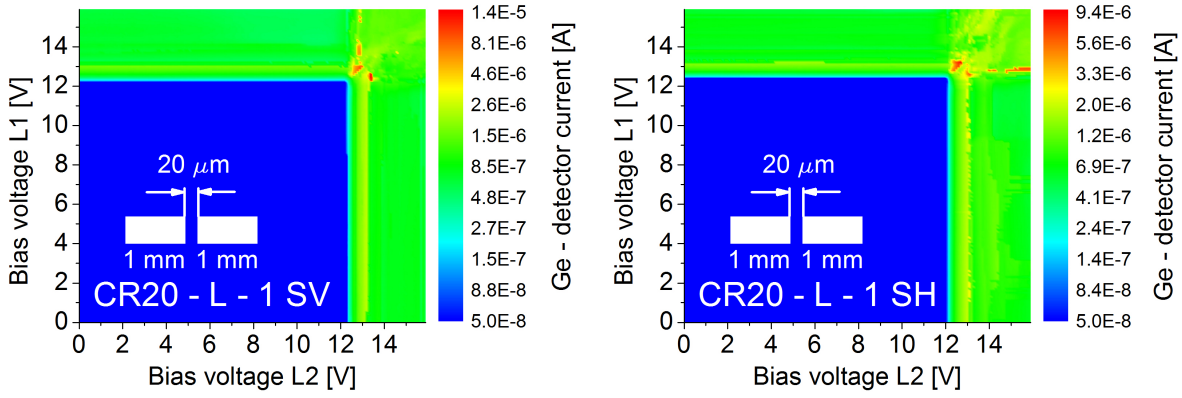

(a) CR20 - L - 1 SV (b) CR20 - L - 1 SH

Figure 5.22.: Coupled ridges CR20.

The SV (a) and SH (b) measurements of coupled ridges in Figure 5.22 show independent lasing emission of both ridges and a maxima at the intersection of both lasing domains. At this crossing point of the bias voltages at about 13 V, the maximum emission has no triangular shape for both ridges pumped above threshold as expected for completely uncoupled ridges in Figure 5.18. The region shows a minimum of radiation at the exact intersection point and no clearly shift of the threshold currents J_{th} to lower bias voltages. This indicates also a weak but present coupling effect even with a 20 μm gap between the facets of the QCL ridges, that was not expected for such "huge" gap sizes. The corresponding characteristic current densities through both devices are shown in Table 5.4

Ridge	L [mm]	Gap size [μm]	J_{th} [A/cm^2] (Bias [V])	J_{max} [A/cm^2] (Bias [V])
L_1	1	20	191.6 (12.23)	265.2 (13)
L_2	1	20	185.2 (12.06)	269.6 (13.07)

Table 5.4.: Coupled ridges CR20

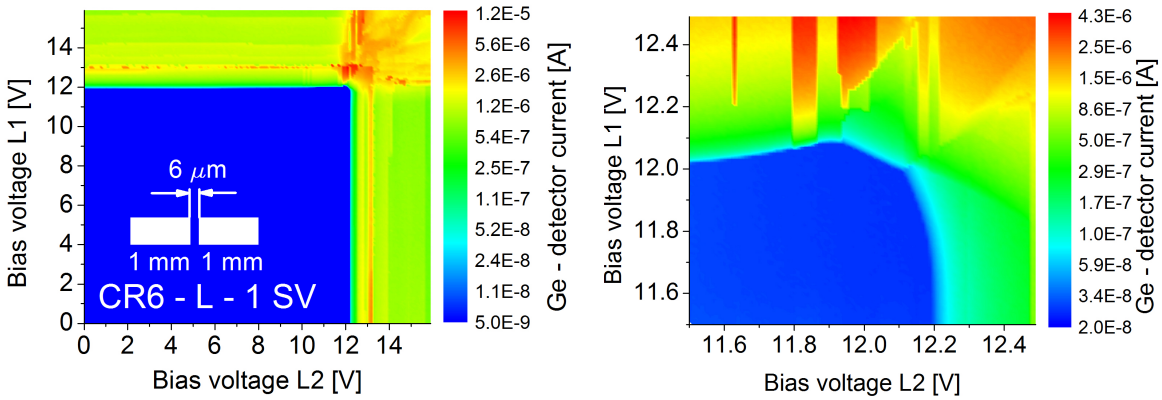

(a) CR6 - L - 1 SV

(b) CR6 - L - 1 SV high resolution

Figure 5.23.: Coupled ridges CR6.

Figure 5.23 (a) shows again the measurement of the coupled ridge configuration with a 6 μm gap and the high resolution measurement near the crossing of the lasing thresholds (b). The threshold of the ridge L_1 increases before the second ridge L_2 reaches its threshold. The shift to higher voltages near the crossing of the lasing domains appears for all different gap sizes. This is exact the opposite behavior of the expected coupling influence, where the threshold should decrease if the second ridge provide no losses to the coupled system. Table 5.5 shows the characteristic current densities for all measured 1mm long QCL ridges.

Ridge	L [mm]	Gap size [μm]	J_{th} [A/cm^2] (Bias [V])	J_{max} [A/cm^2] (Bias [V])
L_1	1	3	188.7 (12)	258 (12.85)
L_2	1	3	188.3 (12)	257.1 (12.85)
L_1	1	6	188 (12)	264 (12.9)
L_2	1	6	188 (12)	267 (13)
L_1	1	10	188 (11.93)	272 (12.97)
L_2	1	10	189.6 (11.95)	271 (12.84)
L_1	1	20	191.6 (12.23)	265.2 (13)
L_2	1	20	185.2 (12.06)	269.6 (13.07)

Table 5.5.: Summarized current densities for the coupled configuration with different gap sizes.

Coupled ridges CR - L - 2.5: $L_1 = L_2 = 2.5$ mm, gap: 3, 6, 10, 20 μm

To analyze the affects of coupling for longer QCL ridge resonators, also ridges with a length of $L_1 = L_2 = 2.5$ mm were measured. Figure 5.24 shows the corresponding plots for different gap sizes. Longer ridges illustrate in principle the same behavior as described for the 1 mm long resonators. The maximum of emission for both ridges is slightly before the intersection of the maximum in the lasing domains of L_1 and L_2. Also for the case of a 20 μm gap and 2.5 mm long ridges a weak coupling is still present. The current density characteristics for this configuration are shown in Table 5.6.

Ridge	L [mm]	Gap size [μm]	J_{th} [A/cm^2] (Bias [V])	J_{max} [A/cm^2] (Bias [V])
L_1	2.5	3	186.4 (12.43)	249.6 (13.47)
L_2	2.5	3	184 (12.4)	240 (13.43)
L_1	2.5	6	186.4 (12.1)	288 (13.3)
L_2	2.5	6	188 (12.3)	277.6 (13.35)
L_1	2.5	10	188 (12.36)	269 (13.4)
L_2	2.5	10	196 (12.46)	279.2 (13.6)
L_1	2.5	20	184 (12.2)	279 (13.48)
L_2	2.5	20	180 (12.3)	277.6 (13.6)

Table 5.6.: Current densities for different coupling configurations of $L_1 = L_2 = 2.5$ mm long ridges and different gap sizes.

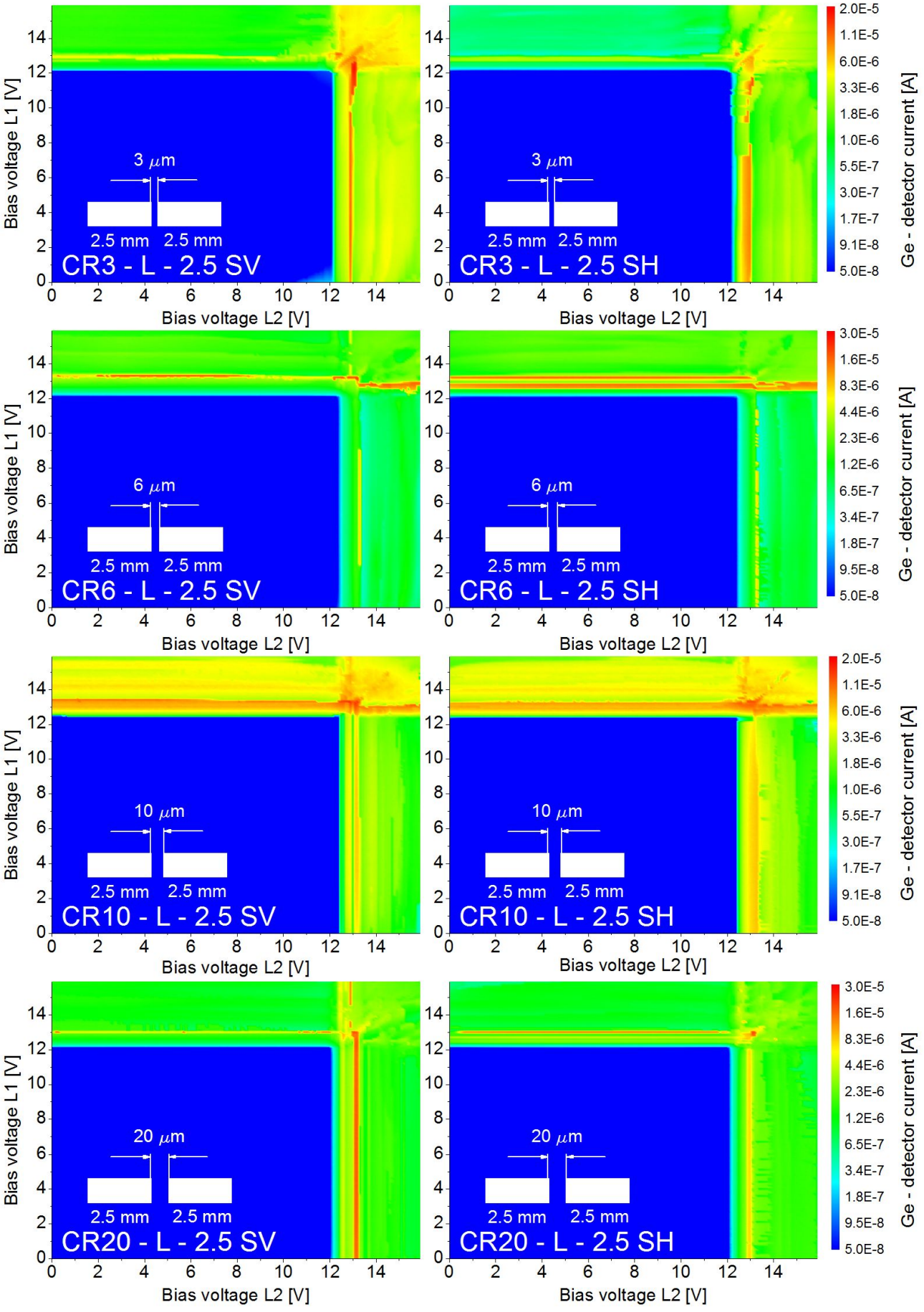

Figure 5.24.: CR - L - 2.5: Coupled ridges

Current change in the 2nd ridge due to lasing:

The recorded data from the 2D measurements were analyzed for current changes in one ridge, when the second is biased. This behavior is shown in Figure 5.25 for the coupled configuration with a gap of 3 μm and $L_1 = L_2 = 1$ mm.

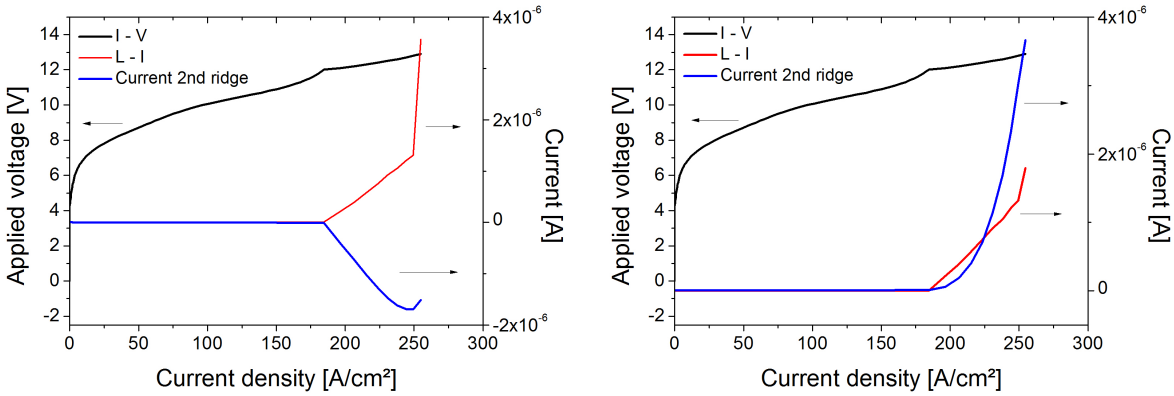

(a) CR3-L-1; 0 V bias voltage

(b) CR3-L-1; 0.5 V bias voltage

Figure 5.25.: Coupled ridges CR3.

Figure 5.25 (a) shows the I - V and L - I of one ridge and the second ridge without bias voltage. When the current density reaches J_{th} and the ridge starts lasing, a negative current is induced in the second ridge which has approximately the same order of magnitude as the detector current. For a small bias voltage of 0.5 V of the second ridge, the current is positive and has a quadratic shape (Fig. 5.25 (b)). The current change in the second ridge indicates exactly the threshold current and this configuration is possible to act as a detector for small gap sizes.

The current change is also depicted for gaps of 6 μm (Fig. 5.26) and 10 μm (Fig. 5.27) between the ridges. There is only a small negative current recognizable at the end of the lasing domain near the NDR region, without a bias voltage in the second ridge. For a small bias voltage of 0.5 V, the measurements of the current show nearly the same behavior as for the small gap of 3 μm. The current in the second ridge is positive and higher compared to the Ge - detector current (Fig. 5.26(b), Fig. 5.27(b)).

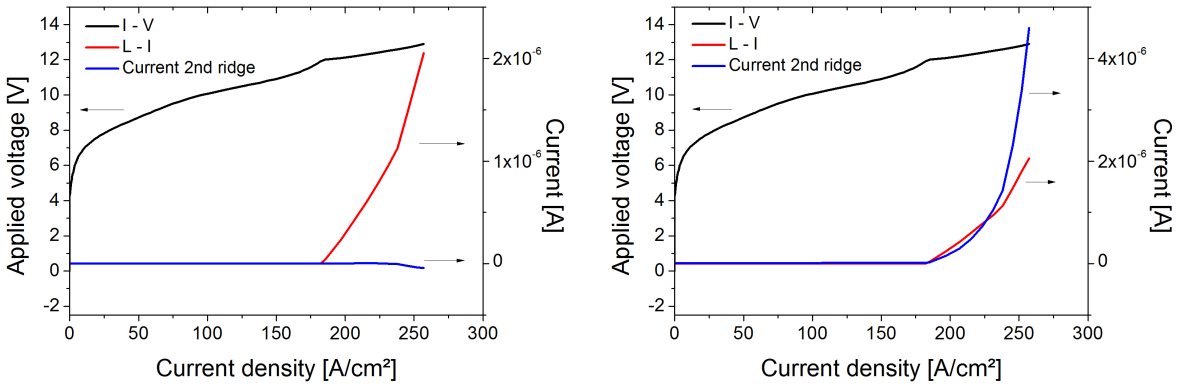

(a) CR6-L-1; 0 V bias voltage

(b) CR6-L-1; 0.5 V bias voltage

Figure 5.26.: Coupled ridges CR6.

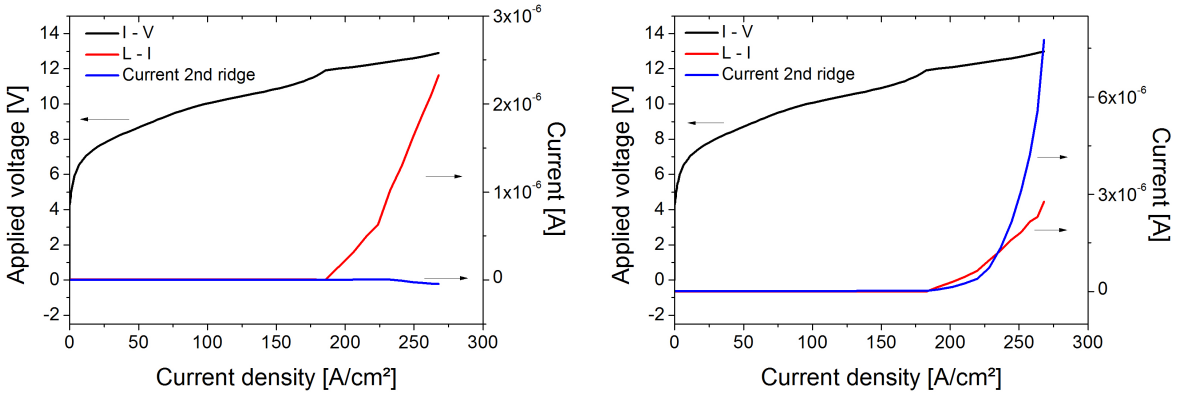

(a) CR10-L-1; 0 V bias voltage

(b) CR10-L-1; 0.5 V bias voltage

Figure 5.27.: Coupled ridges CR10.

The implemented measurements show, that this configuration with two QCL ridges with the same length of $L_1 = L_2 = 1$ mm and a small gap size is possible for one ridge to act as a detector for the second ridge. This current influence reveals the possibility for detector integration on chip and simplifies the measurements due to generation and detection on chip.

6. Summary and outlook

Quantum cascade lasers are promising sources for applications in the THz spectral region. The advantages of this semiconductor lasers are a designable emission frequency, a reasonable output power and the possibility for integration compared to other sources. Therefore, QCLs are interesting coherent sources of THz radiation for further biology, security and material science applications. Unfortunately, no room temperature operation is reached until now, which is the big disadvantage of the devices.

In this thesis the successful design, fabrication and characterization of terahertz quantum cascade lasers has been demonstrated. The design of the terahertz lasers is based on vertical intersubband transitions in a GaAs/AlGaAs heterostructure grown by molecular beam epitaxy (MBE). Resonant longitudinal optical (LO) phonon scattering is used to depopulate the lower lasing level ensuring population inversion. The H256 material system was an existing active region design with a calculated emission frequency of 2.18 THz. A double-metal (DM) waveguide is used for the modal confinement of the disk and ridge resonators.

The characterization of the single disk QCLs at liquid helium temperatures (4.2 K) shows mainly single mode operation from 2 THz to 2.4 THz dependent on the resonator size. The measurements fitted exactly to the simulations of the whispering gallery mode Eigenfrequencies ($n_{eff} = 3.6$) for the different resonators. Continuous mode measurement of coupled disk systems with different radii and gaps of 4 μm and 6 μm between the disks shows similar results compared to the pulsed mode measurements [40]. The possibility to externally control the lasing emission due to the strong intercavity coupling was demonstrated. This coupling depends not only on the gap sizes, also the symmetric or asymmetric sizes of the coupled cavities has an influence.

Continuous mode measurements of coupled ridges with symmetric dimensions and different gaps (3 μm, 6 μm, 10 μm, 20 μm) show also effects of intercavity coupling. Against expectations the ridge resonators has less influence to the intercavity coupling, related to the THz radiation behavior, compared to the disk cavities. It was demonstrated that the frequency mode occurrence, which one wins the gain competition in a ridge resonator, is completely arbitrary for the H256 material system.

The second ridge of a coupled system has indeed measurable current changes dependent on the gap size, when the other ridge is pumped over threshold. This influence enables the possibility to integrate the detector directly on chip.

Removing the bottom gold contact in the gap between the coupled resonators is an idea for future investigations. The performed measurements lead to the assumption, that the layer has an influence of the intercavity coupling between the resonators. Also arrays of several disk or ridge resonators combined to a photonic molecule (PM) are interesting for further investigations.

A. H256 growth sheet

Layer (Substrate → Surface)	X (%)	Thickness (nm)	Doping (Si)
SI GaAs Substrate		$650 \pm 20 \mu m$	
GaAs		300	
AlGaAs	55	150	
Si: GaAs		100	5 e18
Loop 271			
GaAs		9.7	
AlGaAs	15	3.2	
GaAs		16.3	3.5 e15
AlGaAs	15	4.3	
GaAs		7.0	
AlGaAs	15	3.1	
GaAs		8.4	
AlGaAs	15	5.7	
Endloop			
GaAs		9.7	
AlGaAs	15	3.2	
GaAs		16.3	3.5 e15
AlGaAs	15	4.3	
AlGaAs		7.0	
Si:GaAs		60.0	5 e18
Si:InGaAs - 50%In		5.0	2 e19

Table A.1.: Growth sheet of the H256 material.

B. Double - metal processing - cleanroom recipe

The heterostructure wafer with the grown active medium and the n^+ receptor wafer are covered with photoresist to protect from dust, then the active medium samples (1 cm × 1 cm) and the n^+ carrier samples (1.1 cm × 1.1 cm) are cleaved.

Bottom contact metallization and wafer bonding:

Remove protective photoresist and cleaning	Aceton / Isopropanol
Sputter bottom contact Ti/Au	10nm / 1μm
Wafer bonder EVG 501	330 °C / 2000N / 30min

Removing device substrate:

Lap the device	$\approx 50\mu$m remains
Remove remaining substrate	NH_4OH:H_20_2 1 : 20; etch rate $\approx$ 4 μm/min
Remove $Al_{0.55}Ga_{0.45}As$ etch stop layer	HF (38%)

Lithography steps for defining cavities:

Spin photoresist AZ5214	5000 rpm / 35 s
Hotplate	100 °C / 60 s
Boarder exposure	15 s
Developer AZ351 1:5	40 s
Structure exposure	1.5 s
Hotplate	120 °C / 60 s
Flood exposure	15 s

Developer AZ351 1:5	15 s

Top contact metallization:

Sputter top contact Ti/Au	10nm / 500nm
Lift-off	Aceton / Isopropanol

Cavity forming by reactive ion etching (RIE):

Running-in	70min; $SiCl_4$:7 sccm / N_2 :17 sccm,
(with Si carrier in chamber)	RF: 50 W, ICP: 20 W
Structure ecthing	$\approx$ 60min; $SiCl_4$:7 sccm / N_2 :17 sccm,
(etch rate: $\approx$ 300-400nm/min)	RF: 50 W, ICP: 20 W

Bibliography

[1] Yun-Shik Lee. *Principles of Terahertz Science and Technology.* Springer Science+Business Media, 2009.

[2] P. C. Ashworth, E. Pickwell-MacPherson, E. Provenzano, S. E. Pinder, A. D. Purushotham, M. Pepper, and V. P. Wallace. Terahertz pulsed spectroscopy of freshly excised human breast cancer. *Optics Express*, 17(15):12444–12454, 2009.

[3] P. Dean, N. K. Saat, S. P. Khanna, M. Salih, A. Burnett, J. Cunningham, E. H. Linfield, and A. G. Davies. Dual-frequency imaging using an electrically tunable terahertz quantum cascade laser. *Optics Express*, 17(23):20631–20641, 2009.

[4] C.Pflügl, M. A. Belkin, Q. J. Wang, M. Geiser, A. Belyanin, M. Fischer, A. Wittmann, J. Faist, and F. Capasso. Surface-emitting terahertz quantum cascade laser source based on intracavity difference-frequency generation. *Appl. Phys. Lett.*, 93:161110, 2008.

[5] D. T. Hodges, F. B. Foote, and R. D. Reel. Efficient high-power operation of the cw far-infrared waveguide laser. *Appl. Phys. Lett.*, 29:662, 1976.

[6] Anthony E. Siegman. *Lasers.* University Science Books, 1986.

[7] S. M. Sze and Kwok K. Ng. *Physics of Semiconductor Devices - Third Edition.* John Wiley & Sons, 2007.

[8] Günther Bauer and Wolfgang Richter. *Optical Characterization of Epitaxial Semiconductor Layers.* Springer Verlag, 1996.

[9] M. Levinshtein, S. Runyantsev, and Michael Shur. *Handbook series on semiconductor parameters.* World Scientific, 1999.

[10] S. Adachi. *GaAs and related materials: bulk semiconducting and superlattice properties.* World Scientific, 1994.

[11] M. Helm. *Intersubband Transitions in Quantum Wells.* Academic Press, 2000.

[12] J. Faist, F. Capasso, D. L. Sivco, C. Sirtori, A. L. Hutchinson, and A. Y. Cho. Quantum cascade laser. *Science*, 264(5158):553–556, 1994.

[13] Q. Y. Lu, Y. Bai, N. Bandyopadhyay, S. Slivken, and M. Razeghi. Room-temperature continuous wave operation of distributed feedback quantum cascade lasers with watt-level power output. *Appl. Phys. Lett.*, 97(23):231119, 2010.

[14] N. Bandyopadhyay, Y. Bai, B. Gokden, A. Myzaferi, S. Tsao, S. Slivken, and M. Razeghi. Watt level performance of quantum cascade lasers in room temperature continuous wave operation at $\lambda \approx 3.76\mu$m. *Appl. Phys. Lett.*, 97(13):131117, 2010.

[15] R. Köhler, A. Tredicucci, F. Beltram, H. E. Beere, E. H. Linfield, A. G. Davies, D. A. Ritchie, R. C. Iotti, and Fausto Rossi. Terahertz semiconductor-heterostructure laser. *Nature*, 417:156–159, May 2002.

[16] S. Kumar, Q. Hu, and J. L. Reno. 186 K operation of terahertz quantum-cascade lasers based on a diagonal design. *Appl. Phys. Lett.*, 94(13):131105, March 2009.

[17] A. Wade, G. Fedorov, D. Smirnov, S. Kumar, B. S. Williams, Q. Hu, and J. L. Reno. Magnetic-field-assisted terahertz quantum cascade laser operating up to 225 K. *Nature Photonics*, 3:41–45, January 2009.

[18] B. S. Williams. *Terahertz quantum cascade lasers.* PhD thesis, MIT, 2003.

[19] J. H. Smet, C. G. Fonstad, and Q. Hu. Intrawell and interwell intersubband transitions in multiple quantum wells for far-infrared sources. *J. Appl. Phys.*, 79(12):9305–9320, June 1996.

[20] B. S. Williams. Terahertz quantum-cascade lasers. *Nature photonics*, 1:517–525, September 2007.

[21] B. S. Williams, H. Callebaut, S. Kumar, Q. Hu, and J. L. Reno. 3.4 THz quantum cascade laser based on longintudinal-optical-phonon scattering for depopulation. *Appl. Phys. Lett.*, 82(7):1015–1017, 2003.

[22] C. Sirtori, J. Faist, F. Capasso, D. L. Sivco, A. L. Hutchinson, and A. Y. Cho. Quantum cascade laser with plasmon-enhanced waveguide operating at 8.4 μm wavelength. *Appl. Phys. Lett.*, 66:3242–3244, 1995.

[23] C. Sirtori, J. Faist, F. Capasso, D. L. Sivco, A. L. Hutchinson, and A. Y. Cho. Long wavelength infrared ($\lambda \approx 11\mu$m) quantum cascade lasers. *Appl. Phys. Lett.*, 69:2810–2812, 1996.

[24] S. M. Kohen. Electromagnetic modeling of terahertz quantum cascade laser waveguides and resonators. Master's thesis, MIT, 2004.

[25] W. L. Barnes, A. Dereux, and T. W. Ebbesen. Surface plasmon subwavelength optics. *Nature*, 424:824–830, August 2003.

[26] K. Unterrainer, R. Colombelli, C. Gmachl, F. Capasso, H. Y. Hwang, A. M. Sergent, D. L. Sivco, and A. Y. Cho. Quantum cascade lasers with double metal-semiconductor waveguide resonators. *Appl. Phys. Lett.*, 80:3060, 2002.

[27] S. Dhillon et al. Ultralow threshold current terahertz quantum cascade lasers based double-metal buried strip waveguides. *Appl. Phys. Lett.*, 87:071107, 2005.

[28] B. S. Williams, S. Kumar, Q. Hu, and J. L. Reno. Operation of terahertz quantum-cascade lasers at 164 K in pulsed mode and at 117 K in continuous-wave mode. *Opt. Express*, 13:3331–3339, 2005.

[29] S. Kohen, B. S. Williams, and Q. Hu. Electromagnetic modeling of terahertz quantum cascade laser waveguides and resonators. *J. Appl. Phys.*, 97(5):053106, February 2005.

[30] G. Fasching A. Benz, , K. Unterrainer, R. Zobl, A. M. Andrews, T. Roch, W. Schrenk, and G. Strasser. Terahertz microcavity quantum-cascade lasers. *Appl. Phys. Lett.*, 87:211112, 2005.

[31] G. Fasching, V. Tamôsiunas, A. Benz, A. M. Andrews, K. Unterrainer, R. Zobl, T. Roch, W. Schrenk, and G. Strasser. Subwavelength microdisk and microring terahertz quantum-cascade lasers. *IEEE Journal of Quantum Electronics*, 43(8):687–697, August 2007.

[32] G. P. Agrawal and N. K. Dutta. Optical bistability in coupled-cavity semiconductor lasers. *Journal of Applied Physics*, 56(3):664–669, August 1984.

[33] A. Yariv, Y. Xu, R. K. Lee, and A. Scherer. Coupled -resonator optical waveguide: a proposal and analysis. *Optics Letters*, 24(11):711–713, June 1999.

[34] Albert G. and Baca Carol I.H. Ashby. *Fabrication of GaAs Devices.* The Institution of Engineering and Technology, 2005.

[35] O. Manasreh. *Semiconductor Heterojunctions and Nanostructures.* McGraw-Hill Companies, Inc., 2005.

[36] M. H. Herman and H. Sitter. *Molecular Beam Epitaxy - Fundamentals and Current Status.* Springer Verlag, 1996.

[37] M. Fujiwara, N. Hiromoto, H. Shibai, T. Hirao, and T. Nakagawa. Development of far-infrared Ge:Ga photoconductor 2D array for 3 THz imaging. *Proceedings of SPIE*, 4130:842–849, 2000.

[38] A. Rogalski. Infrared detectors: status and trends. *Progress in Quantum Electronics*, 27:59–210, 2003.

[39] D. M. Watson and J. E. Huffman. Germanium blocked impurity band far infrared detectors. *Applied Physics Letters*, 52:1602–1604, 1988.

[40] G. Fasching, C. Deutsch, A. Benz, A. M Andrews, P. Klang, R. Zobl, W. Schrenk, G. Strasser, P. Ragulis, V. Tamosiunas, and K. Unterrainer. Electrically controllable photonic molecule laser. *Opt. Express*, 17(22):20321–20326, October 2009.

[41] M. Martl, J. Darmo, C. Deutsch, M. Brandstetter, A. M. Andrews, P. Klang, G. Strasser, and K. Unterrainer. Gain and losses in thz quantum cascade laser with metal-metal waveguide. *Opt. Express*, 19(2):733–738, January 2011.

Acknowledgments

Bedanken möchte ich mich bei Professor Karl Unterrainer, der mir ermöglicht hat, diese Arbeit durchzuführen und aufgrund seiner langjährigen Erfahrung eine große Hilfe war. Weiters möchte ich mich bei Christoph Deutsch bedanken, der mit mir viel Zeit im Labor verbrachte und mich mit sehr viel Engagement und äußerst aufschlussreichen Diskussionen bei der Durchführung dieser Arbeit stets professionell betreut hat.

Mein besonderer Dank gilt Christina, die mich die letzten Jahre bedingungslos unterstützt hat. Ohne ihren moralischen Beistand, die vielen aufmunternden Worte und ihrer Liebe hätte ich nicht so viel erreicht.

Bedanken möchte ich mich bei meinen Eltern, die mich während meiner gesamten Ausbildung in jeglicher Hinsicht unterstützt, mich jedoch niemals eingeschränkt und mir immer den nötigen Freiraum gelassen haben.

Ausserdem danke ich meinem Studienkollegen Stefan Dornstauder, der mir als Freund während des Studiums an den vielen Tagen des Lernens immer motivierend zur Seite stand, gemeinsam mit mir Projekte verwirklichte und stets ein offenes Ohr für mich hatte.